

Quantum Machine-Learning for Eigenstate Filtration in Two-Dimensional Materials

Manas Sajjan,[†] Shree Hari Sureshbabu,[‡] and Sabre Kais^{*,¶}

[†]*Department of Chemistry, Purdue University, West Lafayette, IN, USA*

[‡]*School of Electrical and Computer Engineering, Purdue University, West Lafayette, IN, USA*

[¶]*Department of Chemistry, Department of Physics and Astronomy, and Purdue Quantum Science and Engineering Institute, Purdue University, West Lafayette, IN, USA*

E-mail: kais@purdue.edu

Abstract

Quantum machine learning algorithms have emerged to be a promising alternative to their classical counterparts as they leverage the power of quantum computers. Such algorithms have been developed to solve problems like electronic structure calculations of molecular systems and spin models in magnetic systems. However the discussion in all these recipes focus specifically on targeting the ground state. Herein we demonstrate a quantum algorithm that can filter any energy eigenstate of the system based on either symmetry properties or on a predefined choice of the user. The work horse of our technique is a shallow neural network encoding the desired state of the system with the amplitude computed by sampling the Gibbs- Boltzmann distribution using a quantum circuit and the phase information obtained classically from the non-linear activation of a separate set of neurons. We show that the resource requirements of our algorithm is strictly quadratic. To demonstrate its efficacy, we use state-filtration in monolayer transition metal-dichalcogenides which are hitherto unexplored in any flavor of quantum

simulations. We implement our algorithm not only on quantum simulators but also on actual IBM-Q quantum devices and show good agreement with the results procured from conventional electronic structure calculations. We thus expect our protocol to provide a new alternative in exploring band-structures of exquisite materials to usual electronic structure methods or machine learning techniques which are implementable solely on a classical computer.

1 Introduction

Machine learning concerned with identifying and utilizing patterns within a data set has gained tremendous importance within the last decade. Even though the germinal idea can be traced back to 1950s,¹ it is safe to say that the domain has become a pioneering field of research within the last few years due to escalation in computational prowess and data availability, and have metamorphosed several disciplines including autonomous driving,² image-recognition,³ speech recognition,⁴ natural language processing,⁵ computer games,⁶ and even refugee integration.⁷ Consequently the integration of the technique in solving problems of physico-chemical interest⁸ have also been explored with remarkable success whether in predicting ground-state density functionals,^{9,10} self-energy in Dynamical Mean-Field Theory (DMFT) for Anderson model,¹¹ atomistic potentials and forcefields for molecular dynamics^{12,13} or unsupervised learning of phases of 2D-Ising Hamiltonian.¹⁴ Similar advancements have also been made in the field of Deep Learning¹⁵ and Artificial Neural Networks (ANN) which has been successfully used to learn phase transition parameters^{16,17} or in quantum phase recognition.¹⁸ Among the various architectures in this category, Restricted Boltzmann machine (RBM) based generative models being a universally powerful approximator for any probability density^{19,20} have particularly arrested attention. RBMs have been successfully used to reconstruct quantum states in tomography from measurement statistics.²¹ Carleo and Troyer showed how a neural network encoding a shallow RBM ansatz requires fewer parameters than certain kind of matrix product states and can predict the ground state

energy and unitary dynamical evolution of simple spin models with high accuracy.²²

However all the algorithms discussed above have trained machine learning or deep-learning models on a classical computer to effectively recreate either a quantum state or its essential features. The past decade have also witnessed unprecedented development in quantum computing as a new paradigm which is fundamentally different than its classical counterpart in processing and storing data and performing logical operations²³ harnessing the power of quantum superposition and non-classical correlations like entanglement. A natural question that has spawned is whether such quantum machines can interpret and produce statistical patterns in data which are either difficult for classical machine learning algorithms or the performance of the latter can be outperformed by the former in efficiency.²⁴ This has naturally motivated the development of a host of quantum -machine learning algorithms like Quantum Principal Component Analysis (PCA),²⁵ Quantum Support Vector Machines (QSVM),²⁶ Quantum Reinforcement Learning,²⁷ quantum supervised and unsupervised learning,²⁸ quantum classifier²⁹ or a plethora of linear algebra routines like HHL,³⁰ QSVD,³¹ qBLAS³² which forms the backbone of the quantum versions of many other machine learning algorithms. Each of these methods have reported theoretical speedup over the best-known classical algorithm under certain specific circumstances.³³ Similar investigations have also been undertaken for artificial neural networks to discover any unforeseen quantum advantage. For instance Amin and co-workers have demonstrated a Quantum Boltzmann Machine³⁴ by adding off-diagonal transverse field to the training model thereby making it more expressive to treat larger classes of problems.³⁵ Weibe *et al* have shown how sampling from a Gibbs distribution as is required for training an RBM can be distinctly accelerated using a quantum processor.³⁶

Motivated by such recent developments, Xia and Kais² proposed an actual quantum circuit using polynomial resources to correctly learn the amplitude of the RBM ansatz encoded within a neural network representing the state of a quantum system. The work also extended the neural network to three layers to learn the sign of the various components of the encoded

wavefunction. The algorithm was benchmarked by showing evaluation of ground states on simple molecular systems like H_2 , LiH etc thereby formally extending the efforts mentioned above to actual electronic structure calculations which are considered to be a powerful applications of near-term quantum devices.³⁸⁻⁴² Kanno *et al.*⁴³ modified the method to encompass the complex phase of each component of the wavefunction by adding an additional neuron to the third layer.

In this paper we focus our attention beyond just the ground state and devise a quantum machine learning algorithm with a three-layered RBM being trained using a quantum circuit to learn any arbitrary state of the system retaining the quadratic resource requirements. We further show the implementation of the algorithm not only on quantum simulator (Qiskit) but on actual NISQ devices using the quantum processors at IBM.⁴⁴ Furthermore unlike most reports on quantum machine learning and quantum computing in general which have studied molecular systems only, we extend the algorithm on important periodic systems quantum simulation of which have just begun to gain attention.^{43,45} Of particular importance in this category are 2D materials like monolayer transition metal di-chalcogenides (TMDCs) which are hitherto unexplored on a quantum computer. These materials have been shown to possess tunable band-gap for many novel applications.⁴⁶⁻⁴⁹ We show how our algorithm can not only learn the true band gap of such materials but can even simulate any state in a unified way depending on user-defined constraints. The importance of understanding excited states for periodic materials underlies its function in photovoltaics^{50,51} and also for other systems can be a generally insightful resource like in elucidating the reaction pathways across conical intersection arising in processes like vision,^{52,53} photosynthesis,^{54,55} magneto-reception^{56,57} and even bio-chemistry of luciferin⁵⁸ etc to name a few. This to the best of our knowledge is first of its kind in any flavors of quantum-machine learning. The results of our algorithm, as shall be discussed, shows excellent agreements with the exact ones even when implemented on an actual noisy quantum computer.

The organization of the paper is as follows. In section 2 we discuss the theoretical under-

pinning of our algorithm with an original proof of feasibility of our cost function employed for training the network. In section 3 we elaborate on the geometry of the network and the details of the algorithm required for learning the desired feature with the concomitant resource requirements and implementation techniques. We prove an explicit lower bound on the probability of successful event on our algorithm (see section 2 Supplementary Information). In section 4 we discuss the application of the algorithm in simulating excited states or any arbitrary states in two important TMDCs- MoS₂ and WS₂ based on user defined constraints. We conclude in section 5 with a brief discussion of possible future extensions.

2 Theory

Our objective is to develop an efficient algorithm to train a neural network to perform the following minimization in a d -dimensional space

$$\min_{\forall \psi \in S} \langle \psi | \hat{H} | \psi \rangle$$

$$S = \{|x\rangle | \hat{O}|x\rangle = \omega|x\rangle \forall |x\rangle \in \mathbb{C}^d\} \quad (1)$$

where $\hat{H} \in \mathbb{C}^{d \times d}$ is the hermitian Hamiltonian defining the problem. Similarly $\hat{O} \in \mathbb{C}^{d \times d}$ is the user-defined hermitian operator. ω is the eigenvalue (real-valued) of the operator \hat{O} and $|x\rangle$ is the corresponding eigenvector. The operators \hat{O} which we shall discuss will generally have more than one elements in set S due to degeneracy in the eigenspace labelled by ω . By construction, the form of the algorithm shall always normalize the state $|\psi\rangle$ and hence normalization as a further constraint is unnecessary. We will return to this point later. The primary goal of the network is to then encode a normalized state-vector $|\psi\rangle$ which is a formal solution to Eq.1 i.e. yield $|\psi\rangle$ from the eigenspace of \hat{O} with eigenvalue ω and among all such possible choices the one with minimum energy.

To solve the quadratic minimization problem with quadratic constraint in Eq.1 we will

define a penalty procedure as

$$F(|\psi\rangle, \hat{H}, \hat{O}, \lambda) = \langle \psi | \hat{H} | \psi \rangle + \lambda \langle \psi | (\hat{O} - \omega)^2 | \psi \rangle \quad (2)$$

where $\lambda \geq 0$ is the penalty parameter. We provide a formal and original proof of equivalence of Eq.S1 with respect to Eq.1 based on the following Theorem.

Theorem 2.1. *Let $\{\lambda_i\}_{i=1}^{\infty}$ be a sequence in the penalty parameter such that $\lambda_1 \leq \lambda_2 \leq \lambda_3 \dots \infty$. Also let $P = \{|\psi_i\rangle\}_{i=1}^{\infty}$ such that $\forall |\psi_i\rangle \in P$ the following is true.*

$$|\psi_i\rangle = \arg \min_{\psi} F(\lambda_i, \hat{H}, \hat{O}, |\psi\rangle) \quad (3)$$

In other words P is the set of minimizers for Eq.S1 for each penalty parameter $\lambda \in \{\lambda_i\}_{i=1}^{\infty}$. If $|\psi^\rangle \in P$ is a limit-point of the convergent sequence $\{|\psi_i\rangle\}_{i=1}^{\infty}$ in P i.e. $|\psi^*\rangle = \lim_{i \rightarrow \infty} |\psi_i\rangle$ then $|\psi^*\rangle \in S$*

An original proof of Theorem 2.1 is in section 1 of the Supporting Information based on the fact that both the 1st and 2nd term in Eq.S1 are quadratic forms. An intuitive explanation can be provided that would suffice to appreciate the discussion in this report. One can note that in the cost function defined in Eq.S1 the term $\langle \psi | \hat{H} | \psi \rangle$ imposes the minimization of energy as required in Eq.1. The second term i.e. $\langle \psi | (\hat{O} - \omega)^2 | \psi \rangle$ is the variance of the operator \hat{O} with the mean being the eigenvalue ω and is non-negative by construction. For large value of penalty parameter λ , the minimization of the overall cost function is afforded if the variance term is pinned to zero i.e. the state $|\psi^*\rangle$ so chosen is an eigenstate of the operator \hat{O} with eigenvalue ω . The space of such states is defined by set S in Eq.1. If several such choices exists, the role of the 1st term kicks in to guarantee optimality in energy.

While optimization schemes with cost functions of the kind in Eq. S1 is beginning

to gain attention in recent literature beyond quantum-machine learning i.e. in algorithms using Unitary-Coupled Cluster Ansatz(UCC) of variational quantum eigensolver (VQE),⁵⁹ a formal proof is lacking. Besides a more popular choice that has been studied in some details is constraining the average value of the operator $\langle\psi|\hat{O}|\psi\rangle$ ^{60,61} with the required eigenvalue instead of penalizing the variance as in Eq.S1. However this recent study⁵⁹ shows Eq.S1 is a better penalty procedure in terms of feasibility and final error than restraining the average without providing a formal proof of equivalence between Eq.S1 and Eq.1. Ref⁵⁹ also implemented the same to target symmetry operators on molecular systems using UCC-VQE using Qulacs⁶² which is an ideal simulator of a real quantum computer. However in this report we shall use Eq. S1 to develop and train a shallow neural network using a quantum machine learning algorithm with quadratic resource requirements in terms of size of qubit register and number of gates. The ansatz which the neural network would encode for the quantum state $|\psi\rangle$ would correspond to a probability density represented by RBM. We benchmark our algorithm on important 2D periodic materials like transition metal dichalcogenides (TMDCs) and show implementations not only on quantum simulators but on actual NISQ device (IBM-Q). TMDCs have never been studied before using any quantum algorithm. In the next few sections we shall show how to filter any specific state of these 2D materials using either symmetry operators of the Hamiltonian or user-defined constructions of operator \hat{O} in a unified manner using the same algorithm. Such an attempt to the best of our knowledge is first of its kind in QML as all previous reports have focused exclusively on targeting the ground state of the system alone.^{43,45}

2.1 Filter for specific excited states

To target the first excited state of the system, one can use in Eq.S1 a user-defined operator ($\hat{O} = |g\rangle\langle g|, \omega = 0$) where $|g\rangle$ is the ground state of the system obtained by training the network in a previous computation with $\lambda = 0$ in Eq.S1. In essence we are requiring the neural-network to return a state-vector in the null space of operator $|g\rangle\langle g|$. Since the null-

space is $d - 1$ dimensional, the minimum energy criterion as enforced by the 1st term in Eq.S1 guarantees the first excited state. This method using the penalty program in Eq.S1 is formally equivalent to deflation technique if one recognizes the idempotency of $\hat{O} = |g\rangle\langle g|$. Deflation has been the cornerstone of many classical algorithms in the past for obtaining excited states^{63,64} and even a quantum algorithm as well with UCC-VQE.⁶⁵ But the formal reduction of our penalty procedure in Eq.S1 based on Theorem 2.1 to deflation offers a slightly different perspective. Moreover as we shall see shortly the penalty program in Eq.S1 is more general and can be used to sieve any state based on arbitrary operator \hat{O} . For higher excited states (say the k th) one can add similar terms to Eq.S1 with the set $\{\hat{O}_i\}_{i=1}^{k-1}$ which forms a set of commuting operators with progressively refined null-space. For the choice of the penalty parameter λ in Eq.S1, one can choose any number greater than the spectral range of the Hamiltonian \hat{H} as that would always work. The spectral range can be computed from the knowledge of the ground state and $\|\hat{H}\|_2$.

2.2 Filter for arbitrary states using symmetry operators

Eq.S1 can be used to solve a more general problem with any symmetry operator of the system \hat{O} (by definition such operators satisfy $[\hat{O}, \hat{H}] = 0$ and hence share the same eigenspace). The corresponding user-desired eigenvalue ω labels the symmetry sector (set S in Eq.1). Unlike in the previous case in section 2.1, usual symmetry operators need not satisfy idempotency and hence relaxation to deflation is impossible. To demonstrate our point, here we shall use $\hat{O} = L^2$ where L^2 is the squared-orbital angular momentum operator, a symmetry for 2D materials. ω would be set to the desired eigenvalue of L^2 . We shall see that the network will always learn the lowest energy eigenstate correctly despite multiple-fold degeneracy. To sieve other states from the entire degenerate subspace one can use a combination filter of $\hat{O}_1 = L^2$ and $\hat{O}_2 = |v\rangle\langle v|$ where $|v\rangle$ is the lowest energy state in the symmetry subspace obtained from the RBM. The penalty parameter λ can be chosen using the prescription in.⁵⁹

3 Algorithm

3.1 The Outline

The RBM network we use in this report consists of three layers each having multiple neurons. The first layer is the visible node consisting of n neurons ($n = \log_2 d$ where d is the dimension of the space as defined in previous section), the second layer is the hidden node consisting of m neurons and the last layer is a phase node consisting of two neurons. The schematic of the entire algorithm and the network architecture is presented in Fig.1(a) and Fig.1(b) respectively. The purpose of the neurons in the phase node is to account for complex values and capture the phase of the wavefunction⁴³ unlike in conventional two-layer RBM networks²¹ which faithfully recovers only the amplitude. Variables encoded by the visible node neurons will be denoted by $\{\sigma_i\}_{i=1}^n$ while those by the hidden node neurons will be denoted by $\{h_j\}_{j=1}^m$. Both σ_i and $h_j \in \{1, -1\}$. The entire algorithm goes as follows. The first step is to initialize the parameters in the network. The bias vector of the visible neurons are denoted as $\vec{a} \in \mathbb{R}^n$, bias vector of hidden neurons are denoted as $\vec{b} \in \mathbb{R}^m$, the interconnecting weights of the visible and hidden neurons are denoted as $\vec{W} \in \mathbb{R}^{n \times m}$. For the phase node, the biases are denoted by $\{c, e\} \in \mathbb{R}^2$ where c is the bias for the neuron capturing the real part of the phase and e is the bias for the neuron encoding the corresponding imaginary part. The phase node shares interconnections with the visible node only and is defined by $\vec{d} \in \mathbb{R}^n$ for the real part of the phase and $\vec{f} \in \mathbb{R}^n$ for the associated imaginary part. Together the set $\vec{X} = (\vec{a}, \vec{b}, \vec{W}, \vec{d}, \vec{f}, c, e)$ defines the complete set of trainable parameters of the model which the network shall learn iteratively. All parameters are randomly initialized in the parameter range $[-0.02, 0.02]$ to avoid vanishing gradient of the activation function for the phase node.² Sometimes if random initialization returns a poorly converged result, we use the initial parameter set of a converged point in a similar problem as the starting guess, a process known as warm optimization.

In the second step the set $(\vec{a}, \vec{b}, \vec{W})$ is fed into the Gibbs sampling circuit shown in

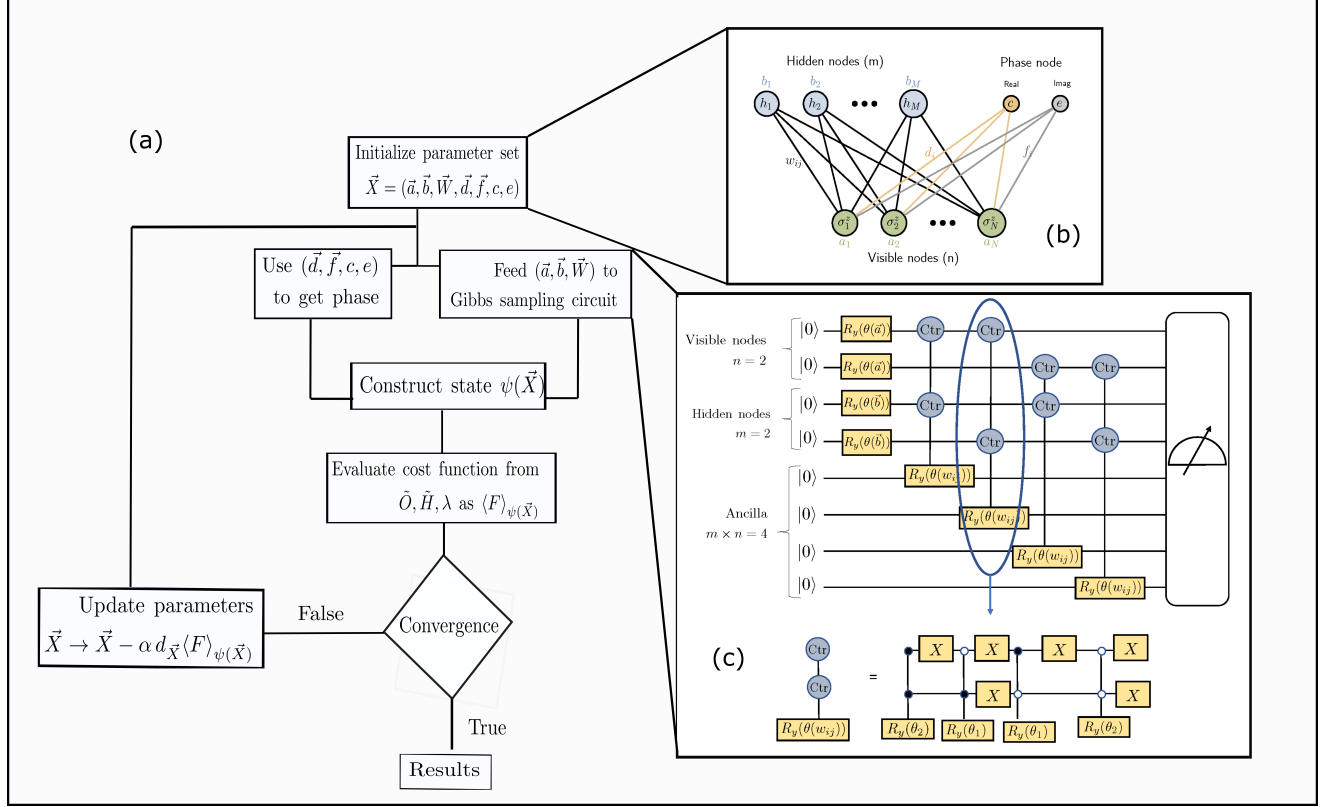


Figure 1: (a) The QML algorithm used to perform the variance penalized optimization. (b) The RBM architecture used in this work. The visible node contains n neurons (green), the hidden node has m neurons (blue) and the phase node contains 2 neuron, one to model the real part(orange) of the phase of the wavefunction and the other to model the imaginary part (grey). The weights and biases of the respective units are displayed. The RBM ansatz for the required state is defined from the Boltzmann distribution over the state-space of the visible units (c) The Gibbs sampling circuit used to create the Boltzmann distribution in (b) for $n = m = 2$. The circuit contains single-qubit R_y gates parameterized by biases of hidden and visible neurons and $C - C - R_y$ gates parameterized by weights between the hidden and visible neurons. Each $C - C - R_y$ gate is conditioned to rotate by different angles θ_1 and θ_2 for different choices of configurations of the control qubits each of which are slightly different function of \vec{W} . This can be implemented by use of X gates as illustrated at the bottom. The open circles show a node in state $|0\rangle$ and the closed circles show a node in state $|1\rangle$. At the end of the circuit all qubits are measured and configurations wherein the ancilla qubits are all in state $|1\rangle$ is post-selected (see text for details)

Fig.1(c). The circuit requires $n + m$ qubits to encode the visible node and the hidden node and respectively and additionally $m \times n$ ancillary qubits. The entire register is initialized to $|0\rangle$. The purpose of the circuit is to sample a bit string $(\vec{\sigma}, \vec{h}) \in \{1, -1\}^{m+n}$ from the distribution $P(\vec{a}, \vec{b}, \vec{W}, \vec{\sigma}, \vec{h})$ defined as

$$P(\vec{a}, \vec{b}, \vec{W}, \vec{\sigma}, \vec{h}) = \frac{e^{\sum_i a_i \sigma_i + \sum_j b_j h_j + \sum_{ij} w_{ij} \sigma_i h_j}}{\sum_{\{\sigma h\}} e^{\sum_i a_i \sigma_i + \sum_j b_j h_j + \sum_{ij} w_{ij} \sigma_i h_j}} \quad (4)$$

In reality the circuit actually draws a sample $(\vec{\sigma}, \vec{h})$ from

$$Q(\vec{a}, \vec{b}, \vec{W}, \vec{\sigma}, \vec{h}) = \frac{e^{\frac{1}{k}(\sum_i a_i \sigma_i + \sum_j b_j h_j + \sum_{ij} w_{ij} \sigma_i h_j)}}{\sum_{\{\sigma h\}} e^{\frac{1}{k}(\sum_i a_i \sigma_i + \sum_j b_j h_j + \sum_{ij} w_{ij} \sigma_i h_j)}} \quad (5)$$

and then reconstruct $P(\vec{a}, \vec{b}, \vec{W}, \vec{\sigma}, \vec{h}) \propto Q(\vec{a}, \vec{b}, \vec{W}, \vec{\sigma}, \vec{h})^k$. The real-valued parameter k will be discussed shortly. The state of the visible node qubits and hidden node qubits are denoted henceforth as $|\sigma_i\rangle$ and $|h_j\rangle$ respectively. Note when σ_i (or h_j) = -1 , $|\sigma_i\rangle$ (or $|h_j\rangle$) = $|0\rangle$ and $|1\rangle$ otherwise. In the circuit shown in Fig.1(c) the single-qubit R_y gates acting only on the visible and hidden units have rotation angles parameterized by (\vec{a}, \vec{b}) and are responsible for creating the non-interacting part of the distribution $Q(\vec{a}, \vec{b}, \vec{W}, \vec{\sigma}, \vec{h})$ while the interaction terms $\{\sum_{i,j} w_{ij} \sigma_i h_j\}$ are turned on through using $C - C - R_y$ acting on ancilla register as the target. The rotation angles of these controlled R_y gates are parameterized by \vec{W} and are different for different configurations of the control qubits (always 1 hidden and 1 visible). Various such choices can be realized by using X gates as shown in Fig.1(c). After all such operations, we measure all the $(m + n + m \times n)$ qubits and post-select the results wherein the ancilla have collapsed to state $|1111\dots 1_{mn}\rangle$ only. We show that the probability of such a successful event have a generic lower bound determinable in terms of the parameters of the network $(\vec{a}, \vec{b}, \vec{W})$ (for details of the derivation of the generic bound refer to section 2 of Supplementary Information). This master lower bound generalizes the previously noted one² as a special case. The role of the real-valued parameter k kicks in here. It serves as a regulator and is chosen in simulation to be $\max(\sum_{ij} \frac{|w_{ij}|}{2}, 1)$ to make the aforesaid lower bound a constant value (see section 2 in Supplementary Information). After the post-selection, the corresponding states of the visible and hidden units is equivalent to all possible bit strings sampled from the distribution $Q(\vec{a}, \vec{b}, \vec{W}, \vec{\sigma}, \vec{h})$ from which the desired distribution $P(\vec{a}, \vec{b}, \vec{W}, \vec{\sigma}, \vec{h})$ is constructed.

With $P(\vec{a}, \vec{b}, \vec{W}, \vec{\sigma}, \vec{h})$ constructed, one can now compute the marginal distribution over the state space of the visible units only as $\tilde{p}(\vec{a}, \vec{b}, \vec{W}, \vec{\sigma})$ where $\tilde{p}(\vec{a}, \vec{b}, \vec{W}, \vec{\sigma}) = \sum_h P(\vec{a}, \vec{b}, \vec{W}, \vec{\sigma}, \vec{h})$.

Now $\sqrt{\tilde{p}(\vec{a}, \vec{b}, \vec{W}, \vec{\sigma})}$ defines the amplitude of wavefunction over basis states of the visible units i.e. $|\sigma_1\sigma_2\dots\sigma_n\rangle$. The phase of each component of the wavefunction is now constructed classically using (\vec{d}, \vec{f}, c, e) and \tanh activation of neurons in the phase node as

$$s(\vec{d}, \vec{f}, c, e, \vec{\sigma}) = \tanh \left[(c + \sum_i d_i \sigma_i) + i(e + \sum_i f_i \sigma_i) \right] \quad (6)$$

With this two information, the target wavefunction can now be constructed as

$$\psi(\vec{X}) = \sum_{\sigma} \sqrt{\tilde{p}(\vec{a}, \vec{b}, \vec{W}, \vec{\sigma})} s(\vec{d}, \vec{f}, c, e, \vec{\sigma}) |\sigma_1\sigma_2\dots\sigma_n\rangle \quad (7)$$

With this wavefunction the cost function in Eq.S1 can now be constructed to check for convergence criterion or maximum number of iterations (to be discussed later). If either criteria is not satisfied then the parameter set \vec{X} is updated using steepest descent algorithm with a learning rate (set to 0.005 in all our calculations) for the next iteration of the algorithm. We have also used ADAM optimizer⁶⁶ but there is no significant change in convergence for the systems treated in this report.

3.2 Resource Requirements

Using n visible neurons and m hidden neurons, a recent study⁶⁷ have shown explicitly how a shallow RBM ansatz ($\alpha = m/n = 1$) like ours already captures several orders of perturbation theory and is a good approximant to the exact state. Classically, constructing such a full RBM distribution will require tracking amplitudes from a 2^{m+n} dimensional state space and hence has exponential resource requirements in preparation. Ref⁶⁸ formalizes and consolidates this statement by proving that a polynomial time algorithm for classically simulating or constructing a full RBM distribution is not only absent now but is unlikely to exist even in future as long as the polynomial hierarchy remains uncollapsed. However such analysis do not preclude the existence of efficient quantum algorithms such as the one considered in this

work.² The Gibbs sampling circuit in our algorithm (see Fig.1(c)) due to representational power of qubits use $m + n + m \times n$ qubits only for constructing the state indicating an $O(m \times n)$ scaling in qubit resource. The gate-set comprising single-qubit R_y gates scales as $m + n$ too, one for each of the visible and hidden node qubits. The $C - C - R_y$ gates are $m \times n$ in number, one for each target ancilla. Toggling between the various configurations of the control qubits (1 visible + 1 hidden) would require 6 R_x gates additionally in each $C - C - R_y$ (see Fig.1(c)) and hence the total number of such R_x gates is $6mn$. This indicates the total gate requirements of our sampling circuit is also $O(m \times n)$. We further prove a master lower bound (see section 2 in Supplementary Information) for successful sampling of our circuit to procure the distribution from which all previously known bounds can be constructed. Quantum advantages such as this have also been observed in supervised learning using RBM distribution.³⁶ The study indicated that for the data-set of size N , a quantum circuit for Gibbs sampling with amplitude amplification reduces the complexity of the algorithm from the conventional $O(N)$ to $O(\sqrt{N})$, a quadratic boast. Furthermore, in this work all our results are compared against exact diagonalization using ‘numpy’ package⁶⁹ in python 3.0 which depending on the LAPACK routine used, usually have a resource scaling of $\simeq O(d^3)$ ⁷⁰ where d as defined before (see section 2) is related to the number of visible neurons n as $n = \log_2 d$. This sets the benchmark for a fair comparison of the resource cost of our method.

3.3 Implementation methods

We implement the algorithm in three flavors of computation. The first flavor henceforth designated as ‘**RBm-cl**’ involves implementing the entire gate set of the Gibbs sampling circuit on a classical computer. This computation returns to us the exact state after the termination of the circuit. The second flavor henceforth designated as ‘**RBm-qasm**’. This has been implemented by simulating the Gibbs sampling circuit using Qiskit which stands for IBM’s Quantum Information Software Kit (Qiskit).⁷¹ We specifically used the *qasm* backend

(hence the name **RBM-qasm**) which is a quantum computer simulator and hence can mimic calculations performed on a noisy-intermediate scale quantum computing device even using a classical computer with options to incorporate customizable noise models. Unlike in ‘**RBM-cl**’ where the exact state is returned, in ‘**RBM-qasm**’, the Gibbs sampling circuit in Fig.1(c) is interrogated multiple times to build measurement statistics. From the observed bit-strings the measurement probabilities $P(\vec{a}, \vec{b}, \vec{W}, \vec{\sigma}, \vec{h})$ is computed and hence the results are subjected to statistical fluctuations due to finite sampling errors. No noise model was used during the simulation in ‘**RBM-qasm**’. Finally to see the effect of noise we also investigated the performance of our algorithm on real IBM-Q quantum computers using the Qiskit interface. We used IBM-Q Sydney⁷² and IBM-Q Toronto⁷³ interchangeably both of which are 27 qubit machines and hence suitable for our case studies. Calculations of this flavor are henceforth referred to as ‘**RBM-IBMQ**’. To reduce the effect of noise on the sampling probabilities we employ the same noise mitigation procedure as has been used by the authors recently.^{45,71} For the ‘**RBM-qasm**’ and ‘**RBM-cl**’ simulations, the maximum number of iterations within which well-converged results to be discussed below were obtained is $\leq 30,000$ either with a warm-start or randomly initialized parameter set depending on the case. The ‘**RBM-IBMQ**’ simulations were performed in batches with maximum iteration ≤ 700 for each run to reduce job queue.

4 Results and Discussion

As a test of our method we target state filtration of energy eigenstates of two well-established transition-metal dichalcogenides (TMDCs) - monolayer Molybdenum di-Sulfide (MoS₂) and monolayer Tungsten di-Sulfide (WS₂). Monolayer TMDCs have so far eluded attention in quantum simulations even though it is imperative to study their electronic structures to understand novel properties^{49,74} like high carrier mobility, high photoluminescence due to direct-band gap, lack of inversion symmetry leading to large spin-orbit coupling and intra-

valley transport etc. Indeed such features have made them attractive candidates for applications in Field-Effect Transistors,⁷⁵ supercapacitors,⁷⁶ spintronics,⁷⁷ opto-electronics,^{78,79} valleytronics.⁸⁰ We first show how the entire conduction band (CB) in such materials can be simulated using an appropriate choice of operator \hat{O} as the ground state projector as discussed before and then later show how to ‘sieve’ eigenstates based on angular momentum symmetry. In all cases, we implement our algorithm on three flavors of RBM calculations - RBM-cl, RBM-qasm, RBM-IBMQ as discussed.

4.1 Filter for target excited states- Simulation of conduction band in MoS₂ and WS₂

The geometrical structure of monolayer TMDCs like MoS₂ or WS₂ indicates the presence of a trigonal prismatic unit cell with D_{3h} point group symmetry.⁴⁹ The transition metal is at the centre and the sulfur atoms are at the six corners of the triangular prism. Consequently, the best orbital decomposition to evaluate the band structure of this periodic material should involve not only the s, p, d -orbitals of the central metal atom but also of the surrounding sulfur atoms. Indeed several reports exist which treats the electronic structure of such materials using a tight-binding description obtainable from a 5 band, 7-band or an 11-band model using varying degree of inclusion of the orbital set of the metal and the chalcogen.⁸¹⁻⁸⁴ However, recently a 3-band parameterization have been demonstrated to yield remarkable accuracy in energy over the entire Brillouin zone.³ A tight binding Hamiltonian in this description is obtained by fitting the energy curves against DFT calculations (with GGA and LDA functionals) employing the d_{z^2} , d_{xy} and $d_{x^2-y^2}$ orbitals of the metal centre³ only. This choice is based on the fact that for trigonal prismatic co-ordination, the d-orbital set of the metal splits into three groups- A'_1 containing d_{z^2} orbital only, E' containing $d_{xy}, d_{x^2-y^2}$ and E'' containing d_{xz}, d_{yz} orbitals. However reflection symmetry of D_{3h} restricts inter-coupling between the orbitals of E'' set with the remaining two groups. Indeed E'' contributes exclusively to higher energy bands and have no role to play in the low-energy physics of the

valence and conduction band which is considered in this work. Absence of chalcogen p -orbitals is definitely an approximation albeit a good one as seen from Ref.³ We shall return to this point shortly.

We use a tight-binding model comprising of third-nearest neighbor (TNN) metal-metal hopping³ of the aforesaid three band Hamiltonian for all our calculations henceforth. The parameters of the model are obtained from the more accurate GGA calculation set.³ Section 3 of Supplementary Information enlist details of the Hamiltonian and parameters for completeness and brevity. Our working Hamiltonian, for both the systems is thus a 3×3 Hermitian matrix. For qubitization we convert it into a 4×4 Hermitian matrix by padding an additional 1×1 block with a diagonal entry chosen to be \geq spectral range of $H_{3 \times 3}$ as that would keep the low-lying eigenvalue structure of the resultant matrix undisturbed for the training to successfully proceed. Thus for both the systems, our neural network comprises of a visible node with 2 neurons to encode the state, two hidden neurons and additional 2 neurons for the phase node too. For the Gibbs sampling circuit in Fig.1(c), we thus need 2 qubits to represent the entire visible layer and 2 qubits for the hidden layer. In addition we need 4 ancilla qubits to serve as targets for $(C - C - R_y)$ rotation making the total qubit count to 8. For the circuit in Fig.1(c), we use 4 single qubit Rotation gates (R_y), 4 Controlled-Controlled Rotation gates $(C - C - R_y)$, and also 24 Bit-flip (X) gates. The optimization in each case starts from a randomly initialized parameter set. In case if the self-convergence is poor, we re-start the algorithm by feeding the initial parameter from the results of a nearby converged k -point as a warm start. We see the results are in excellent agreement with the exact diagonalization when a such a warm start is employed along with *Measurement Error Mitigation*. For IBMQ implementation we have used ‘IBM-Sydney’ and ‘IBM-Toronto’ both of which are 27 qubit machines. To reduce the operational time on the actual quantum device for job queue and isolate the effect of gate-infidelity, IBMQ simulations for each k -point were often warm-started with an initial parameter set obtained from the initial parameters of the *qasm* simulation of a nearby but non-identical k -point.

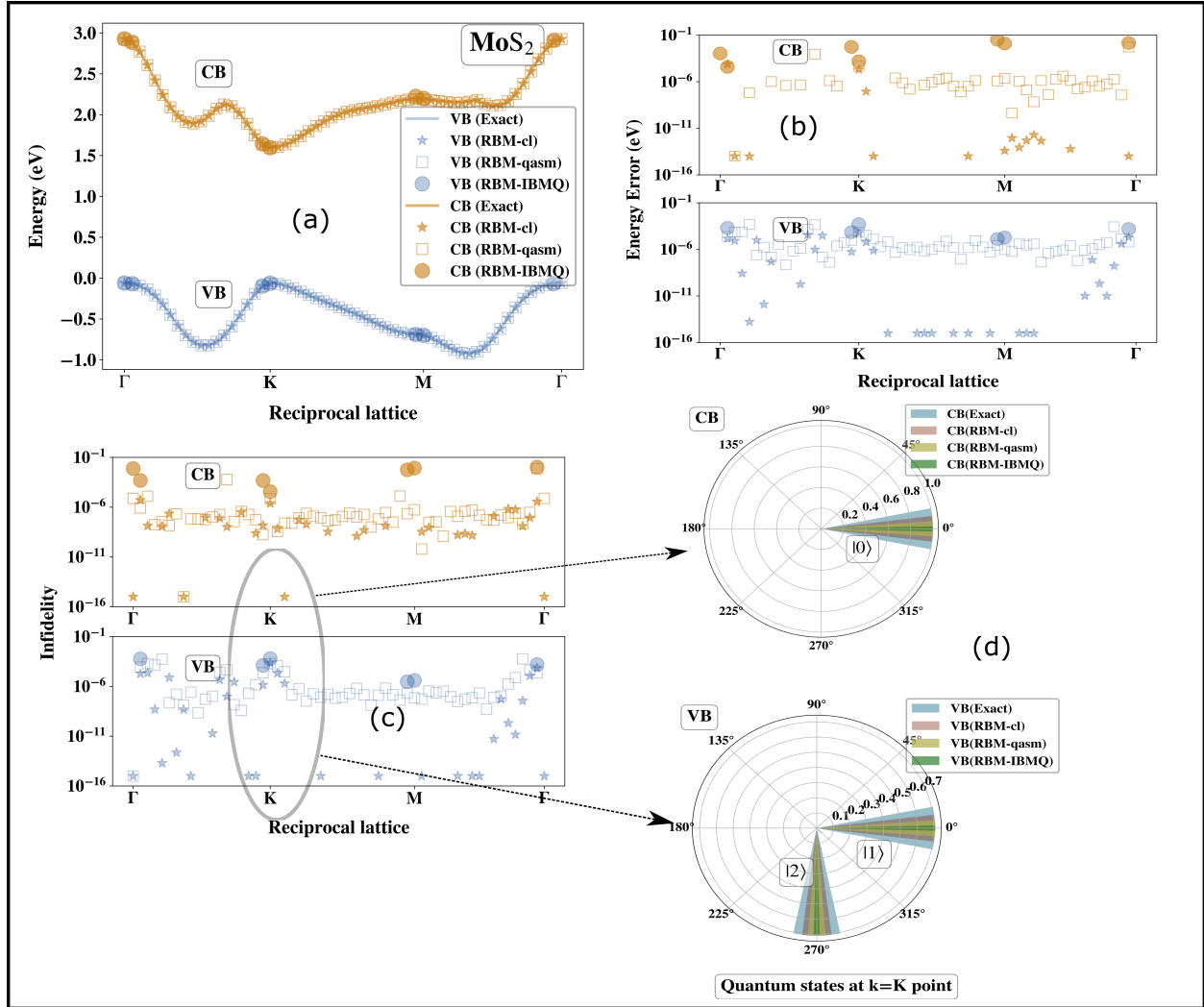


Figure 2: (a) Valence (VB) and conduction band (CB) of MoS₂ calculated using all flavors of RBM and overlaid against exact diagonalization. The valence band is simulated using $\lambda = 0$ in Eq.S1 and the conduction band using ($O = |v_0\rangle\langle v_0|$, $\omega = 0$, $\lambda = 5$) in Eq.S1 where $|v_0\rangle$ is the valence band state at each k-point. For IBMQ implementations we used ‘IBM-Sydney’ and ‘IBM-Toronto’. All parameters are randomly initialized (see Fig.1) or warm-started with the initial guess of a converged nearby k-point (b) The corresponding energy errors from (a) in eV (c) The corresponding state infidelities ($1-Fid$) where $Fid = |\langle \Psi_{RBM} | \Psi_{Exact} \rangle|^2$ (d) The orbital decomposition of the states at K -point where $|0\rangle = d_{z^2}$, $|1\rangle = d_{xy}$, $|2\rangle = d_{x^2-y^2}$. The states from RBM calculations matches well with those from exact diagonalization in phase and amplitude. The width for each bar is set differently for visual clarity.

The results from the algorithm using the cost function in Eq.S1 is displayed in Fig.2 for MoS₂ and Fig.3 for WS₂. In Fig.2(a) we have overlaid the energies obtained from our algorithm as a function of the wave-vector index sampled from the Brillouin zone following the usual $\Gamma - K - M - \Gamma$ path. The result for the valence band (VB) is denoted in blue and is obtained by setting $\lambda = 0$ in Eq.S1 which corresponds to the usual variational optimization

to obtain the ground state at each k-point. The results for the conduction band (CB) are shown in orange in Fig.2(a). They are thereafter computed as a separate set of calculations using $O = |v_0\rangle\langle v_0|$ and $\omega = 0$ in the cost function in Eq.S1 where the corresponding ground state in the valence band (VB) is denoted as $|v_0\rangle$. The penalty parameter is $\lambda = 5$. The cost-function now samples a state orthogonal to ground state (null space of the projector $|v_0\rangle\langle v_0|$) for each of the k-points. The minimum energy criterion imposed by the first term in the cost function in Eq.S1 guarantees obtaining the next higher excited state which happens to be the state space in the conduction band.

We see for all flavors of our algorithm (RBM-cl, RBM-qasm, RBM-IBMQ) the simulated energy values for both the valence and the conduction band are in good agreement with the ones obtained from exact diagonalization. The corresponding errors in energy is displayed in Fig.2(b) and is usually $\leq 10^{-4}$ eV for RBM-cl and RBM-qasm which are noiseless pristine implementations but is around $10^{-2} - 10^{-4}$ eV for the valence band (VB) and the conduction band for RBM-IBMQ indicating the worsening of performance due to faulty gate implementations in the Gibbs sampling circuit. Fig.2(c) plots the state infidelities i.e. $1-Fid$ where $Fid = |\langle \Psi_{\text{RBM}} | \Psi_{\text{Exact}} \rangle|^2$. We see that the infidelities are also quite small for each band with the performance worsened only in the IBMQ variant of the RBM implementation.

Like Fig.2(a), Fig.3(a) displays the band structure of WS_2 wherein the energies for both the valence and conduction band are overlayed against the energy values obtained from exact diagonalization. All three flavors of RBM implementation yields reasonably accurate results as in the case for Fig.2(a). Fig.3(b) and Fig.3(c) displays the energy error and the state infidelities of the state obtained from the RBM calculations against exact diagonalization. The error ranges in each case is similar to what has been discussed for MoS_2 .

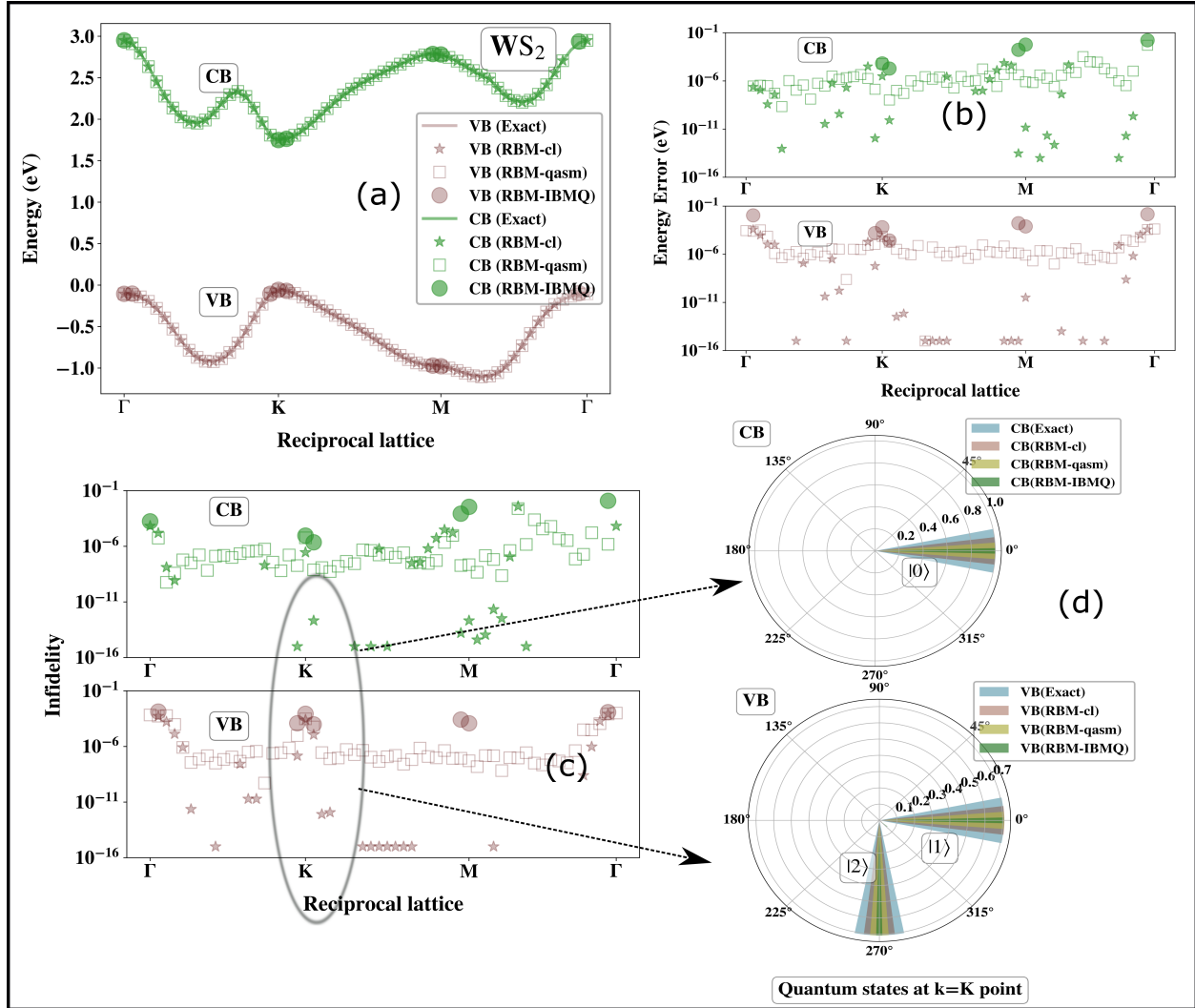


Figure 3: (a) Valence (VB) and conduction band (CB) of WS₂ calculated using all flavors of RBM and overlaid against exact diagonalization. The valence band is simulated using $\lambda = 0$ in Eq.S1 and the conduction band using $(O = |v_0\rangle\langle v_0|, \omega = 0, \lambda = 5)$ in Eq.S1 where $|v_0\rangle$ is the valence band state at each k-point. For IBMQ implementations we used ‘IBM-Sydney’ and ‘IBM-Toronto’. All parameters are randomly initialized (see Fig.1) or warm-started with the initial guess of a converged nearby k-point (b) The corresponding energy errors from (a) in eV (c) The corresponding state infidelities ($1-Fid$) where $Fid = |\langle \Psi_{RBM} | \Psi_{Exact} \rangle|^2$ (d) The orbital decomposition of the states at K -point where $|0\rangle = d_{z^2}$, $|1\rangle = d_{xy}$, $|2\rangle = d_{x^2-y^2}$. The states from RBM calculations matches well with those from exact diagonalization in phase and amplitude. The width for each bar is set differently for visual clarity.

Fig. 2(d) and Fig. 3(d) displays the orbital decomposition of the states in the conduction and valence band at the most important symmetry point i.e. the K - point. In our calculations qubit $|0\rangle = d_{z^2}$, $|1\rangle = d_{xy}$, $|2\rangle = d_{x^2-y^2}$ where $\{0, 1, 2\}$ are the integer equivalents of the two-qubit bit strings encoding the neurons of the visible node. We see from our calculations however that the exact state generated from the model lines up correctly against the RBM

states in both amplitude and phase. While the state of the conduction band at K -point is exclusively populated by the d_{z^2} , that in the valence band is a superposition of d_{xy} and $d_{x^2-y^2}$ with a phase shift of $3\pi/2$. This is consistent with the orbital decomposition given in Fig.2 of Ref³ and is partly the reason given by the authors to use this three orbitals for generating the tight-binding Hamiltonian as the model yields correct state description near the band-gap. However as is clear from Fig.2 of Ref,³ the orbital composition of the states at the Γ and M -point has contribution from the p-orbitals of S and s-orbitals of both the metal and the S atoms. This makes the three-band model an approximation for the exact character of the states even though it can replicate the energy very well throughout the Brillouin zone.

4.2 Filter for arbitrary states using symmetry operators

In this section we shall use the same set of TMDCs discussed above to explore how one can sieve arbitrary states based on symmetry constraints. To demonstrate the point we use orbital angular momentum symmetry. The L_z operator in the three-band approximation commutes with the Hamiltonian³ in absence of spin-orbit coupling as has been considered in this work. The operators L_x, L_y are essentially null matrices in the three-band basis of $\{d_{z^2}, d_{xy}, d_{x^2-y^2}\}$ as mentioned in.³ Hence L^2 enjoys exclusive contribution from L_z and is a symmetry operator in the system. For computation, we use the Hamiltonian of the system at the K -point because the three-band approximation as discussed before is extremely accurate therein.

The complete set of eigenvalues and eigenstates of L_z and hence of L^2 operator is given in section 4 of Supplementary Information. From the knowledge of the spectrum of L^2 operator we see that it has two distinct eigenvalues which are $\{0, 4\}$ in atomic units. One of eigenvectors of the doubly-degenerate eigenspace with eigenvalue 4 is the state in the valence band and the other is a higher energy excited state above the conduction band (not shown in Fig.2 or in Fig.3). Both these states are exclusively made from the contribution of $\{d_{xy}, d_{x^2-y^2}\}$ as seen from the state decomposition in section 4 of the Supplementary

Information. The sector with eigenvalue 0 has single-fold degeneracy and is made from the excited state in the conduction band. As discussed before in Fig.2(d) and Fig.3(d) (also in section 4 of Supplementary Information) this state is exclusively made from the contribution of the d_{z^2} which explains the absence of z-component angular momentum. We would thus expect that if we choose $\hat{O} = L^2$ and $\omega = \{0, 4\}$ in Eq.S1 for training the network, we should yield the excited state in the conduction band for $\omega = 0$ and should yield the ground state in the valence band for $\omega = 4$ as that is of lower energy (in compliance with the first term in Eq.S1) than the other degenerate eigenstate.

The qubit and gate resource requirements of this simulation is exactly the same as discussed in section 4.1 with 2 visible node neurons and 2 hidden node neurons for each of the two systems MoS₂ and WS₂. The Gibbs sampling circuit in Fig.1(c) would need a total of 8 qubits as before (2 for visible node + 2 for hidden node + 4 ancillary qubits). The gate requirements for the circuit to reproduce the amplitude is thus 4 single qubit Rotation gates (R_y), 4 Controlled-Controlled Rotation gates ($C - C - R_y$) and also 24 Bit-flip (X) gates. We start the optimization with randomly initialized parameters.

In Fig.4 we display the results of our simulation. Like before, the results from all three flavors of RBM (marked as 2 = RBM-cl, 3 = RBM-qasm and 4 = RBM-IBMQ) are compared against the exact expected state (marked as 1 = Exact). In Fig.4(a), the results of energy in eV from the three RBM simulations and the exact one is displayed for the eigenvalue sector $\omega = 0$ a.u. This happens to be the conduction band (CB) energy in Fig.2(a). We find an extremely good agreement for all flavors of RBM with the exact value. The corresponding energy error is displayed in Fig.4(c) and is in the range of $10^{-5} - 10^{-4}$ eV for RBM-cl and RBM-qasm but is within $10^{-4} - 10^{-3}$ eV for the RBM-IBMQ variant. Fig.4(b) displays the constraint violation error i.e. how much the state encoded in the neural network after training has an $\langle L^2 \rangle$ equal to the target value of ω (in this case $\omega = 0$ a.u.). We see that the violations are quite small for the noiseless implementations. Even for implementation on actual NISQ devices of IBM-Q, it is close to 10^{-3} a.u.

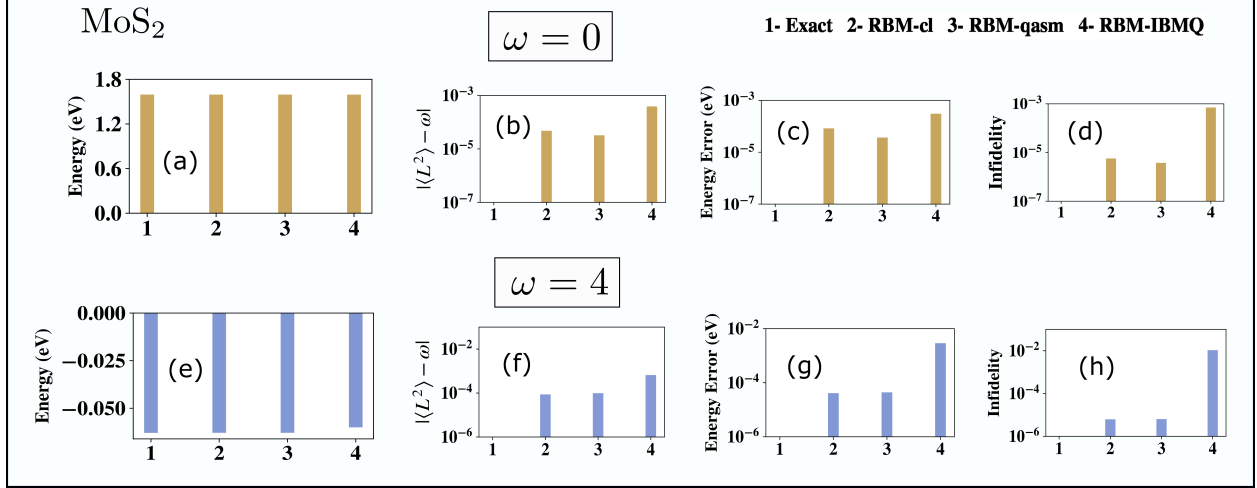


Figure 4: (a) The energy comparison between exact(1), RBM-cl(2), RBM-qasm(3), RBM-IBMQ(4) for computation with $\hat{O} = L^2$ and eigenvalue $\omega = 0.0$ a.u. in Eq.S1. The exact energy is 1.5950 eV and is the conduction band energy at K -point in MoS₂ shown in Fig.2 (b) The constraint violation error $|\langle L^2 \rangle - \omega|$ of the state obtained from different flavors of RBM and the desired value ω (c) The energy error in eV from (a) of the states obtained from RBM (d) The state infidelities ($1-Fid$ where $Fid = |\langle \Psi_{\text{RBM}} | \Psi_{\text{Exact}} \rangle|^2$) obtained from RBM and the exact one (e-h) corresponds to an equivalent set of plots as in (a-d) just described but with the other eigenspace of L^2 with eigenvalue $\omega = 4$ a.u. The exact energy here is the valence band energy at K -point for MoS₂ shown in Fig.2 and is -0.0629 eV

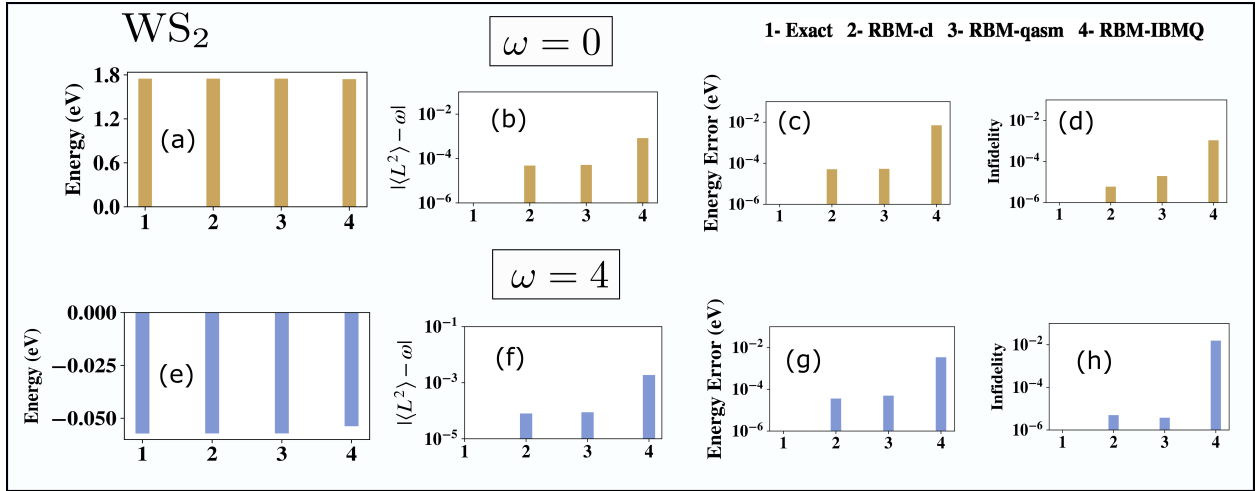


Figure 5: (a) The energy comparison between exact(1), RBM-cl(2), RBM-qasm(3), RBM-IBMQ(4) for computation with $\hat{O} = L^2$ and eigenvalue $\omega = 0.0$ a.u. in Eq.S1. The exact energy is 1.749 eV and is the conduction band energy at K -point in WS₂ shown in Fig.3 (b) The constraint violation error $|\langle L^2 \rangle - \omega|$ of the state obtained from different flavors of RBM and the desired value ω (c) The energy error in eV from (a) of the states obtained from RBM (d) The state infidelities ($1-Fid$ where $Fid = |\langle \Psi_{\text{RBM}} | \Psi_{\text{Exact}} \rangle|^2$) obtained from RBM and the exact one (e-h) corresponds to an equivalent set of plots as in (a-d) just described but with the other eigenspace of L^2 with eigenvalue $\omega = 4$ a.u. The exact energy here is the valence band energy at K -point for WS₂ shown in Fig.3 and is -0.0572 eV

Fig.4(d) displays the state infidelity error ($1-Fid$ where $Fid = |\langle \Psi_{\text{RBM}} | \Psi_{\text{Exact}} \rangle|^2$). We

see that for all flavors of RBM implementation the infidelities are quite small with the performance worsened for implementation on the actual IBM-Q device. Fig.4(e-h) corresponds to similar plots as discussed above but this time in the other eigenvalue sector with $\omega = 4$ a.u. We again see that the energy values (in eV) in Fig.4(e) matches with the exact for all flavors of RBM-implementation. This state happens to be the ground state in the valence band (VB) shown in Fig.2(a). The corresponding energy errors shown in Fig.2(g) are like in the previous case low for RBM-cl and RBM-qasm but in the range of $10^{-3} - 10^{-2}$ eV for RBM-IBMQ. Similar analysis as in the case of $\omega = 0$ a.u. can also be made for the constraint violation error Fig.2(f) and the state infidelity Fig.2(h). Both of these have low errors with the respective ranges as displayed.

Fig.5 shows a similar plot for the other system studied WS_2 . Just as before we display the results for $\omega = 0$ a.u. in Fig.5(a-d) and for $\omega = 4$ a.u. in Fig.5(e-h). Fig.5(a) shows the energy match between the RBM implementations and the exact value for $\omega = 0$ a.u. and Fig.5(e) shows the same for $\omega = 4$ a.u. The former is equal to the state in the conduction band at K -point (see Fig.3(a)) and the latter is the corresponding state in the valence band (see Fig.3(a)). We see good agreement for all RBM variants and the exact expected value. The corresponding energy errors are low (see Fig.5(c) and Fig.5(g)) with the range for IBMQ implementation being $10^{-3} - 10^{-2}$ eV and even lesser for the pristine implementations. The respective constraint violation errors are displayed in Fig.5(b) and Fig.5(f) and are small too as seen from the scale. Similar statement can also be made for the state infidelity displayed in Fig.5(d) and Fig.5(h). We have seen that in both the systems MoS_2 and WS_2 , the state infidelity be higher in the $\omega = 4$ a.u. eigensector than in $\omega = 0$ a.u. eigensector in the IBMQ implementation especially. In fact the relative energy errors for the said sector is close to 5% for RBM-IBMQ. However the corresponding errors (both relative and absolute) is low for the noiseless implementation (RBM-cl and RBM-qasm) indicating that the higher % error is attributable to imperfect implementation of gates in the Gibbs sampling circuit in an IBM-Q machine and hence can be mitigated with future quantum computing devices with better

gate fidelities and error-correction schemes.

5 Conclusion

In this study we have demonstrated an algorithm which can filter arbitrary energy eigenstates in 2D materials like TMDCs using a quantum circuit with quadratic resources. We provided an original proof of feasibility for our cost function employed for the constrained optimization. We also proved a generic lower bound for the successful sampling of our quantum circuit from which previously known bounds can be extracted. Our circuit trains a three-layered neural network that encodes the desired state using an RBM ansatz for the probability density. As an illustration, we were able to filter energy eigenstates in the conduction band of important TMDCs like MoS₂ and WS₂ and faithfully reproduce the band gap. We were also able to filter arbitrary states based on a user defined orbital angular momentum symmetry constraint. We trained the network on various flavors of computation using not only a classical computer, *qasm* backend quantum simulator in Qiskit but also a real IBMQ machine (IBM Sydney and IBM Toronto) with the objective to see the performance of the algorithm on actual NISQ devices. In all flavors of computation our algorithm demonstrated very high accuracy when compared to the exact values obtained from direct diagonalization.

Venturing beyond the ground state to obtain arbitrary states based on user-defined restrictions is first of its kind in all flavors of QML. Furthermore the systems of our choice happens to be TMDCs, an important class of 2D-periodic systems which have never been studied using any quantum algorithm. Periodic systems in general have received scanty attention as far as quantum algorithms are concerned. Only two reports exists^{43,45} both of which have simulated just the valence band in graphene and hexagonal Boron Nitride (h-BN). Further extension of this algorithm can be made to compute operators using Hellmann-Feynmann method,⁸⁷ to characterize the influence of noise on the algorithm and to see it being extended to study other interesting phenomenon on 2D materials like spin-orbit interaction

due to inversion symmetry breaking^{49,88} and Rashba splitting in polar TMDCs⁸⁹ or even effect of strain.⁹⁰ From the algorithmic point of view, besides being quadratic scaling in qubit and gate requirements, our algorithm does not have any dependence on oracular objects like qRAM³³ which is responsible for creating a superposition of all possible basis states and is known to commonly sought in most quantum machine learning modules. As futuristic quantum devices are being developed with proper error mitigation schemes, we expect to have more such cross-pollination between machine learning algorithms and quantum computing with the promise to study electronic structure and dynamics in new complex materials.

6 Data and model availability

The information about the input Hamiltonian and L^z/L^2 operator corresponding to MoS₂ and WS₂ can be found in the Supplementary Information in section 3 and 4 respectively. Data will be made available upon reasonable request to the corresponding author. The codes associated with the classical simulation, simulation on the *qasm* backend, and the implementation on IBM’s quantum computing devices is available with the corresponding author upon reasonable request.

Acknowledgement

We would like to thank Dr. Ruth Pachter, AFRL, for many useful discussions. AFRL support is acknowledged. We would also like to thank Sangchul Oh for his help during the preparation of the manuscript. We would like to acknowledge the support from National Science Foundation under award number 1955907. This material is also based upon work supported by the U.S. Department of Energy, Office of Science, National Quantum Information Science Research Centers. We also acknowledge the use of IBM-Q and thank them for the support. The views expressed are those of the authors and do not reflect the official policy or position of IBM or the IBM Q team.

References

- (1) Cohen, S. Chapter 1 - The evolution of machine learning: past, present, and future. In Artificial Intelligence and Deep Learning in Pathology; Cohen, S., Ed.; Elsevier, 2021; pp 1–12.
- (2) Chen, C.; Seff, A.; Kornhauser, A.; Xiao, J. DeepDriving: Learning Affordance for Direct Perception in Autonomous Driving. 2015 IEEE International Conference on Computer Vision (ICCV). 2015; pp 2722–2730.
- (3) He, K.; Zhang, X.; Ren, S.; Sun, J. Deep residual learning for image recognition. Proceedings of the IEEE conference on computer vision and pattern recognition. 2016; pp 770–778.
- (4) Sak, H.; Senior, A.; Rao, K.; Irsoy, O.; Graves, A.; Beaufays, F.; Schalkwyk, J. Learning acoustic frame labeling for speech recognition with recurrent neural networks. 2015 IEEE international conference on acoustics, speech and signal processing (ICASSP). 2015; pp 4280–4284.
- (5) Hoy, M. B. Alexa, Siri, Cortana, and More: An Introduction to Voice Assistants. Medical reference services quarterly **2018**, 37, 81–88.
- (6) Silver, D. et al. Mastering the game of Go with deep neural networks and tree search. Nature **2016**, 529, 484–489.
- (7) Bansak, K.; Ferwerda, J.; Hainmueller, J.; Dillon, A.; Hangartner, D.; Lawrence, D.; Weinstein, J. Improving refugee integration through data-driven algorithmic assignment. Science **2018**, 359, 325–329.
- (8) Carleo, G.; Cirac, I.; Cranmer, K.; Daudet, L.; Schuld, M.; Tishby, N.; Vogt-Maranto, L.; Zdeborová, L. Machine learning and the physical sciences. Rev. Mod. Phys. **2019**, 91, 45002.

- (9) Snyder, J. C.; Rupp, M.; Hansen, K.; Müller, K.-R.; Burke, K. Finding Density Functionals with Machine Learning. Phys. Rev. Lett. **2012**, 108, 253002.
- (10) Brockherde, F.; Vogt, L.; Li, L.; Tuckerman, M. E.; Burke, K.; Müller, K.-R. Bypassing the Kohn-Sham equations with machine learning. Nature Communications **2017**, 8, 872.
- (11) Arsenault, L. F.; Lopez-Bezanilla, A.; Von Lilienfeld, O. A.; Millis, A. J. Machine learning for many-body physics: The case of the Anderson impurity model. Physical Review B - Condensed Matter and Materials Physics **2014**, 90, 1–16.
- (12) Bartók, A. P.; Payne, M. C.; Kondor, R.; Csányi, G. Gaussian Approximation Potentials: The Accuracy of Quantum Mechanics, without the Electrons. Phys. Rev. Lett. **2010**, 104, 136403.
- (13) Li, Z.; Kermode, J. R.; De Vita, A. Molecular dynamics with on-the-fly machine learning of quantum-mechanical forces. Physical Review Letters **2015**, 114, 1–5.
- (14) Wang, L. Discovering phase transitions with unsupervised learning. Physical Review B **2016**, 94, 2–6.
- (15) Lecun, Y.; Bengio, Y.; Hinton, G. Deep learning. Nature **2015**, 521, 436–444.
- (16) Carrasquilla, J.; Melko, R. G. Machine learning phases of matter. Nature Physics **2017**, 13, 431–434.
- (17) Ch’Ng, K.; Carrasquilla, J.; Melko, R. G.; Khatami, E. Machine learning phases of strongly correlated fermions. Physical Review X **2017**, 7, 1–9.
- (18) Cong, I.; Choi, S.; Lukin, M. D. Quantum convolutional neural networks. Nature Physics **2019**, 15, 1273–1278.
- (19) Le Roux, N.; Bengio, Y. Representational Power of Restricted Boltzmann Machines and Deep Belief Networks. Neural Computation **2008**, 20, 1631–1649.

- (20) Melko, R. G.; Carleo, G.; Carrasquilla, J.; Cirac, J. I. Restricted Boltzmann machines in quantum physics. Nature Physics **2019**, 15, 887–892.
- (21) Torlai, G.; Mazzola, G.; Carrasquilla, J.; Troyer, M.; Melko, R.; Carleo, G. Neural-network quantum state tomography. Nature Physics **2018**, 14, 447–450.
- (22) Carleo, G.; Troyer, M. Solving the quantum many-body problem with artificial neural networks. Science **2017**, 355, 602–606.
- (23) Preskill, J. Quantum Computing in the NISQ era and beyond. Quantum **2018**, 2, 79.
- (24) Biamonte, J.; Wittek, P.; Pancotti, N.; Rebentrost, P.; Wiebe, N.; Lloyd, S. Quantum machine learning. Nature **2017**, 549, 195–202.
- (25) Lloyd, S.; Mohseni, M.; Rebentrost, P. Quantum principal component analysis. Nature Physics **2014**, 10, 631–633.
- (26) Rebentrost, P.; Mohseni, M.; Lloyd, S. Quantum support vector machine for big data classification. Physical review letters **2014**, 113, 130503.
- (27) Dunjko, V.; Taylor, J. M.; Briegel, H. J. Quantum-Enhanced Machine Learning. Physical Review Letters **2016**, 117, 1–6.
- (28) Lloyd, S.; Mohseni, M.; Rebentrost, P. Quantum algorithms for supervised and unsupervised machine learning. arXiv preprint arXiv:1307.0411 **2013**,
- (29) Neven, H.; Denchev, V. S.; Rose, G.; Mcready, W. G. Training a large scale classifier with the quantum adiabatic algorithm. arXiv preprint arXiv:0912.0779 **2009**,
- (30) Harrow, A. W.; Hassidim, A.; Lloyd, S. Quantum Algorithm for Linear Systems of Equations. Phys. Rev. Lett. **2009**, 103, 150502.
- (31) Rebentrost, P.; Steffens, A.; Marvian, I.; Lloyd, S. Quantum singular-value decomposition of nonsparse low-rank matrices. Phys. Rev. A **2018**, 97, 12327.

- (32) Cui, X.; Shi, Y. QBLAS : A Quantum Basic Linear Algebra and Simulation Library.
- (33) Ciliberto, C.; Herbster, M.; Ialongo, A. D.; Pontil, M.; Rocchetto, A.; Severini, S.; Wossnig, L. Quantum machine learning: a classical perspective. arXiv **2017**,
- (34) Amin, M. H.; Andriyash, E.; Rolfe, J.; Kulchytskyy, B.; Melko, R. Quantum Boltzmann Machine. Physical Review X **2018**, 8.
- (35) Kieferová, M.; Wiebe, N. Tomography and generative training with quantum Boltzmann machines. Phys. Rev. A **2017**, 96, 62327.
- (36) Wiebe, N.; Kapoor, A.; Svore, K. M. Quantum deep learning. arXiv preprint arXiv:1412.3489 **2014**,
- (2) Xia, R.; Kais, S. Quantum machine learning for electronic structure calculations. Nature Communications **2018**, 9, 4195.
- (38) Aspuru-Guzik, A.; Dutoi, A. D.; Love, P. J.; Head-Gordon, M. Simulated Quantum Computation of Molecular Energies. Science **2005**, 309, 1704–1707.
- (39) Kais, S. Introduction to Quantum Information and Computation for Chemistry. In Quantum Information and Computation for Chemistry; John Wiley & Sons, Ltd, 2014; Chapter 1, pp 1–38.
- (40) Peruzzo, A.; McClean, J.; Shadbolt, P.; Yung, M.-H.; Zhou, X.-Q.; Love, P. J.; Aspuru-Guzik, A.; O’Brien, J. L. A variational eigenvalue solver on a photonic quantum processor. Nature Communications **2014**, 5, 4213.
- (41) Kandala, A.; Mezzacapo, A.; Temme, K.; Takita, M.; Brink, M.; Chow, J. M.; Gambetta, J. M. Hardware-efficient variational quantum eigensolver for small molecules and quantum magnets. Nature **2017**, 549, 242.
- (42) Daskin, A.; Kais, S. Direct application of the phase estimation algorithm to find the eigenvalues of the Hamiltonians. Chemical Physics **2018**, 514, 87–94.

- (43) Kanno, S.; Tada, T. Many-body calculations for periodic materials via restricted Boltzmann machine-based VQE. Quantum Science and Technology **2021**, 6, 25015.
- (44) Aleksandrowicz, G.; Alexander, T.; Barkoutsos, P.; Bello, L.; Ben-Haim, Y.; Bucher, D.; Cabrera-Hernández, F. J.; Carballo-Franquis, J.; Chen, A.; Chen, C. F.; Others, Qiskit: An open-source framework for quantum computing. Accessed on: Mar 2019, 16.
- (45) Sureshbabu, S. H.; Sajjan, M.; Oh, S.; Kais, S. Implementation of Quantum Machine Learning for Electronic Structure Calculations of Periodic Systems on Quantum Computing Devices. arXiv **2021**, 1–31.
- (46) Choi, W.; Choudhary, N.; Han, G. H.; Park, J.; Akinwande, D.; Lee, Y. H. Recent development of two-dimensional transition metal dichalcogenides and their applications. Materials Today **2017**, 20, 116–130.
- (47) Liu, M.; Liu, W.; Liu, X.; Wang, Y.; Wei, Z. Application of transition metal dichalcogenides in mid-infrared fiber laser. Nano Select **2021**, 2, 37–46.
- (48) Lv, R.; Robinson, J. A.; Schaak, R. E.; Sun, D.; Sun, Y.; Mallouk, T. E.; Terrones, M. Transition Metal Dichalcogenides and Beyond: Synthesis, Properties, and Applications of Single- and Few-Layer Nanosheets. Accounts of Chemical Research **2015**, 48, 56–64.
- (49) Manzeli, S.; Ovchinnikov, D.; Pasquier, D.; Yazyev, O. V.; Kis, A. 2D transition metal dichalcogenides. Nature Reviews Materials **2017**, 2.
- (50) Li, C.; Cao, Q.; Wang, F.; Xiao, Y.; Li, Y.; Delaunay, J.-J.; Zhu, H. Engineering graphene and TMDs based van der Waals heterostructures for photovoltaic and photoelectrochemical solar energy conversion. Chem. Soc. Rev. **2018**, 47, 4981–5037.
- (51) Alharbi, F. H.; Kais, S. Theoretical limits of photovoltaics efficiency and possible improvements by intuitive approaches learned from photosynthesis and quantum coherence. Renewable and Sustainable Energy Reviews **2015**, 43, 1073–1089.

- (52) Palczewski, K. Chemistry and biology of vision. Journal of Biological Chemistry **2012**, 287, 1612–1619.
- (53) Tapavicza, E.; Tavernelli, I.; Rothlisberger, U. Trajectory Surface Hopping within Linear Response Time-Dependent Density-Functional Theory. Phys. Rev. Lett. **2007**, 98, 23001.
- (54) Cerullo, G.; Polli, D.; Lanzani, G.; De Silvestri, S.; Hashimoto, H.; Cogdell, R. J. Photosynthetic Light Harvesting by Carotenoids: Detection of an Intermediate Excited State. Science **2002**, 298, 2395–2398.
- (55) Hu, Z.; Engel, G. S.; Kais, S. Double-excitation manifold's effect on exciton transfer dynamics and the efficiency of coherent light harvesting. Phys. Chem. Chem. Phys. **2018**, 20, 30032–30040.
- (56) Rodgers, C. T.; Hore, P. J. Chemical magnetoreception in birds: The radical pair mechanism. Proceedings of the National Academy of Sciences **2009**, 106, 353–360.
- (57) Zhang, Y.; Berman, G. P.; Kais, S. Sensitivity and entanglement in the avian chemical compass. Phys. Rev. E **2014**, 90, 42707.
- (58) Chung, L. W.; Hayashi, S.; Lundberg, M.; Nakatsu, T.; Kato, H.; Morokuma, K. Mechanism of efficient firefly bioluminescence via adiabatic transition state and seam of sloped conical intersection. Journal of the American Chemical Society **2008**, 130, 12880–12881.
- (59) Kuroiwa, K.; Nakagawa, Y. O. Penalty methods for a variational quantum eigensolver. Physical Review Research **2021**, 3, 21–24.
- (60) Ryabinkin, I. G.; Genin, S. N.; Izmaylov, A. F. Constrained Variational Quantum Eigensolver: Quantum Computer Search Engine in the Fock Space. Journal of Chemical Theory and Computation **2019**, 15, 249–255.

- (61) Greene-Diniz, G.; Muñoz Ramo, D. Generalized unitary coupled cluster excitations for multireference molecular states optimized by the variational quantum eigensolver. International Journal of Quantum Chemistry **2021**, 121, 1–20.
- (62) Suzuki, Y. et al. Qulacs: a fast and versatile quantum circuit simulator for research purpose. **2020**,
- (63) Miranda-Quintana, R. A.; González, M. M. Deflation techniques in quantum chemistry: Excited states from ground states. International Journal of Quantum Chemistry **2013**, 113, 2478–2488.
- (64) Hemmatiyani, S.; Sajjan, M.; Schlimgen, A. W.; Mazziotti, D. A. Excited-State Spectra of Strongly Correlated Molecules from a Reduced-Density-Matrix Approach. The Journal of Physical Chemistry Letters **2018**, 9, 5373–5378, PMID: 30183311.
- (65) Higgott, O.; Wang, D.; Brierley, S. Variational Quantum Computation of Excited States. Quantum **2019**, 3, 156.
- (66) Kingma, D. P.; Ba, J. L. Adam: A method for stochastic optimization. 3rd International Conference on Learning Representations, ICLR 2015 - Conference Track Proceedings **2015**, 1–15.
- (67) Borin, A.; Abanin, D. A. Approximating power of machine-learning ansatz for quantum many-body states. Phys. Rev. B **2020**, 101, 195141.
- (68) Long, P. M.; Servedio, R. A. Restricted Boltzmann Machines are hard to approximately evaluate or simulate. ICML 2010 - Proceedings, 27th International Conference on Machine Learning **2010**, 703–710.
- (69) Harris, C. R. et al. Array programming with NumPy. Nature **2020**, 585, 357–362.
- (70) Blackford, S. LAPACK Benchmark. 1999; <http://www.netlib.org/lapack/lug/node71.html>.

- (71) Abraham, H. et al. Qiskit: An Open-source Framework for Quantum Computing. 2019.
- (72) 27-qubit backend: "IBMQ Team, IBM Q 27 Sydney backend specification V1.0.46,". 2021; <https://quantum-computing.ibm.com>.
- (73) 27-qubit backend: "IBMQ Team, IBM Q 27 Toronto backend specification V1.4.25,". 2021; <https://quantum-computing.ibm.com>.
- (74) Yang, L.; Xie, C.; Jin, J.; Ali, R. N.; Feng, C.; Liu, P.; Xiang, B. Properties, Preparation and Applications of Low Dimensional Transition Metal Dichalcogenides. Nanomaterials **2018**, 8.
- (75) Bao, W.; Cai, X.; Kim, D.; Sridhara, K.; Fuhrer, M. S. High mobility ambipolar MoS₂ field-effect transistors: Substrate and dielectric effects. Applied Physics Letters **2013**, 102, 42104.
- (76) Choudhary, N.; Patel, M. D.; Park, J.; Sirota, B.; Choi, W. Synthesis of large scale MoS₂ for electronics and energy applications. Journal of Materials Research **2016**, 31, 824–831.
- (77) Ahn, E. C. 2D materials for spintronic devices. npj 2D Materials and Applications **2020**, 4, 17.
- (78) Mak, K. F.; Lee, C.; Hone, J.; Shan, J.; Heinz, T. F. Atomically Thin MoS₂: A New Direct-Gap Semiconductor. Phys. Rev. Lett. **2010**, 105, 136805.
- (79) Gong, C.; Zhang, Y.; Chen, W.; Chu, J.; Lei, T.; Pu, J.; Dai, L.; Wu, C.; Cheng, Y.; Zhai, T.; Li, L.; Xiong, J. Electronic and Optoelectronic Applications Based on 2D Novel Anisotropic Transition Metal Dichalcogenides. Advanced Science **2017**, 4, 1700231.
- (80) Mak, K. F.; Xiao, D.; Shan, J. Light valley interactions in 2D semiconductors. Nature Photonics **2018**, 12, 451–460.

- (81) Ridolfi, E.; Le, D.; Rahman, T. S.; Mucciolo, E. R.; Lewenkopf, C. H. A tight-binding model for MoS₂ monolayers. Journal of Physics: Condensed Matter **2015**, 27, 365501.
- (82) Zahid, F.; Liu, L.; Zhu, Y.; Wang, J.; Guo, H. A generic tight-binding model for monolayer, bilayer and bulk MoS₂. AIP Advances **2013**, 3, 52111.
- (83) Shahriari, M.; Ghalambor Dezfuli, A.; Sabaeian, M. Band structure and orbital character of monolayer MoS₂ with eleven-band tight-binding model. Superlattices and Microstructures **2018**, 114, 169–182.
- (84) Fang, S.; Kuate Defo, R.; Shirodkar, S. N.; Lieu, S.; Tritsarlis, G. A.; Kaxiras, E. Ab initio tight-binding Hamiltonian for transition metal dichalcogenides. Phys. Rev. B **2015**, 92, 205108.
- (3) Liu, G. B.; Shan, W. Y.; Yao, Y.; Yao, W.; Xiao, D. Three-band tight-binding model for monolayers of group-VIB transition metal dichalcogenides. Physical Review B - Condensed Matter and Materials Physics **2013**, 88, 1–11.
- (86) neural networks. **2017**, 606, 602–606.
- (87) Oh, S. Quantum computational method of finding the ground-state energy and expectation values. Phys. Rev. A **2008**, 77, 12326.
- (88) Zhu, Z. Y.; Cheng, Y. C.; Schwingenschlögl, U. Giant spin-orbit-induced spin splitting in two-dimensional transition-metal dichalcogenide semiconductors. Phys. Rev. B **2011**, 84, 153402.
- (89) Yao, Q.-F.; Cai, J.; Tong, W.-Y.; Gong, S.-J.; Wang, J.-Q.; Wan, X.; Duan, C.-G.; Chu, J. H. Manipulation of the large Rashba spin splitting in polar two-dimensional transition-metal dichalcogenides. Phys. Rev. B **2017**, 95, 165401.

- (90) Peng, Z.; Chen, X.; Fan, Y.; Srolovitz, D. J.; Lei, D. Strain engineering of 2D semiconductors and graphene: from strain fields to band-structure tuning and photonic applications. Light: Science and Applications **2020**, 9.

Supplementary Information for Quantum Machine-Learning for Eigenstate Filtration in Two-Dimensional Materials

1 Proof of Theorem 2.1

The proof of feasibility of general penalty functions is known in optimization theory. Since both our objective function and penalty term are quadratic forms herein we construct an original and a formal proof for Theorem 2.1.

Let us recollect the cost function $F(\lambda, \hat{H}, \hat{O}, |\psi\rangle)$ defined in text:

$$F(\lambda, \hat{H}, \hat{O}, |\psi\rangle) = \langle \psi | \hat{H} | \psi \rangle + \lambda \langle \psi | (\hat{O} - \omega)^2 | \psi \rangle \quad (\text{S1})$$

1.1 Definitions

We re-iterate the following definitions as considered in the main text

1. $\hat{H} \in \mathbb{C}^{d \times d}$ and $\hat{H} = \hat{H}^\dagger$. This is the Hamiltonian operator in the problem and we denote the spectrum of \hat{H} by $\vec{\sigma} = [\sigma_0, \sigma_1, \dots, \sigma_n]^T$ where $\sigma_0 \leq \sigma_1 \leq \dots \leq \sigma_n$. We shall assume that the entries of \hat{H} in the chosen basis is finite.
2. $\hat{O} \in \mathbb{C}^{d \times d}$ and $\hat{O} = \hat{O}^\dagger$ is an user-defined operator for the problem. ω is an eigenvalue of operator \hat{O} . We denote the spectrum of operator $(\hat{O} - \omega)^2$ as $\vec{\eta} = [\eta_0, \eta_1, \eta_2, \dots, \eta_n]^T$ where $\eta_0 \leq \eta_1 \leq \eta_2, \dots \leq \eta_n$. Further $\eta_i \geq 0 \forall i$ as $(\hat{O} - \omega)^2 \succeq 0$ (positive-semidefinite by construction)
3. $\text{Null}(\hat{A}) = \{|x\rangle \mid \hat{A}|x\rangle = 0, \forall |x\rangle \in \mathbb{C}^d\}$ where \hat{A} is any arbitrary operator $\in \mathbb{C}^{d \times d}$.
4. $\lambda \in \mathbb{R}_{++}$ is a penalty parameter
5. $|\psi\rangle \in \mathbb{C}^d$ is the state-vector of the system sought from the minimization scheme by training the neural network.

6. $\{\lambda_i\}_{i=1}^{\infty}$ is a sequence in the penalty parameter such that $\lambda_1 \leq \lambda_2 \leq \lambda_3 \dots \infty$

7. $P = \{|\psi_i\rangle\}_{i=1}^{\infty}$ such that $\forall |\psi_i\rangle \in P$ the following is true.

$$|\psi_i\rangle = \arg \min_{\psi} F(\lambda_i, \hat{H}, \hat{O}, |\psi\rangle) \quad (\text{S2})$$

In other words P is the set of minimizers for Eq.S1 for each penalty parameter $\lambda \in \{\lambda_i\}_{i=1}^{\infty}$.

8. $|\psi^*\rangle = \lim_{i \rightarrow \infty} |\psi_i\rangle$ be the limit point of a convergent sequence in P

9. All vectors $\in \mathbb{C}^d$ discussed below will be considered normalized unless otherwise stated

Using the definitions above we construct the following lemmas.

Lemma 1. For any $|\psi\rangle \in \mathbb{C}^d$, $\langle\psi|\hat{A}|\psi\rangle \leq \sqrt{\text{Tr}(\hat{A}^\dagger\hat{A})}$ where \hat{A} is any arbitrary hermitian operator $\in \mathbb{C}^{d \times d}$.

Proof. Let us denote the variance of operator \hat{A} as $\text{Var}(\hat{A})$ evaluated in an arbitrary state $|\psi\rangle \in \mathbb{C}^d$. $\text{Var}(\hat{A})$ by definition is always non-negative. From this we can claim

$$\begin{aligned} \text{Var}(\hat{A}) &= \langle\psi|\hat{A}^2|\psi\rangle - (\langle\psi|\hat{A}|\psi\rangle)^2 \geq 0 \quad \because \text{(by definition)} \\ \langle\psi|\hat{A}^2|\psi\rangle &\geq (\langle\psi|\hat{A}|\psi\rangle)^2 \\ \langle\psi|\hat{A}^\dagger\hat{A}|\psi\rangle &\geq (\langle\psi|\hat{A}|\psi\rangle)^2 \quad \because (\hat{A} = \hat{A}^\dagger) \end{aligned} \quad (\text{S3})$$

Now let us consider a complete set of eigenvectors of $\hat{A}^\dagger\hat{A}$ denoted as $\{|s_i\rangle\}_{i=1}^d$ with corresponding eigenvalues $\{s_i\}_{i=1}^d$ which are non-negative as $\hat{A}^\dagger\hat{A} \succeq 0$. One can resolve the state $|\psi\rangle$ in the basis $\{|s_i\rangle\}_{i=1}^d$ as follows

$$|\psi\rangle = \sum_{i=1}^d \langle s_i|\psi\rangle |s_i\rangle \quad (\text{S4})$$

Using Eq.S4 to express $\langle\psi|\hat{A}^\dagger\hat{A}|\psi\rangle$ we have

$$\begin{aligned} &\langle\psi|\hat{A}^\dagger\hat{A}|\psi\rangle \\ &= \sum_{i=1}^d s_i |\langle s_i|\psi\rangle|^2 \\ &\leq \sum_{i=1}^d s_i \quad \because s_i \geq 0 \text{ and } 0 \leq |\langle s_i|\psi\rangle|^2 \leq 1 \\ &= \text{Tr}(\hat{A}^\dagger\hat{A}) \end{aligned} \quad (\text{S5})$$

We can thus make the following claim

$$\begin{aligned}
& \text{Tr}(\hat{A}^\dagger A) \\
& \geq \langle \psi | \hat{A}^\dagger \hat{A} | \psi \rangle \quad \because \text{Eq.S5} \\
& \geq (\langle \psi | \hat{A} | \psi \rangle)^2 \quad \because \text{Eq.S3} \\
\implies \langle \psi | \hat{A} | \psi \rangle & \leq \sqrt{\text{Tr}(\hat{A}^\dagger A)} \tag{S6}
\end{aligned}$$

□

Lemma 2. $|\psi^*\rangle \in P$ and is a limit-point of the convergent sequence in P if $\langle \psi^* | (\hat{O} - \omega)^2 | \psi^* \rangle = 0$

Proof. Let us consider a state $|\psi'\rangle \in S$, where the set S is defined as

$$S = \{|x\rangle | \hat{O}|x\rangle = \omega|x\rangle \ \forall |x\rangle \in \mathbb{C}^d\} \tag{S7}$$

The following is then true

$$\langle \psi' | \hat{H} | \psi' \rangle = \langle \psi' | \hat{H} | \psi' \rangle + \lambda_k \langle \psi' | (\hat{O} - \omega)^2 | \psi' \rangle \quad \because |\psi'\rangle \in S \tag{S8}$$

$$= F(\lambda_k, \hat{H}, \hat{O}, |\psi'\rangle) \tag{S9}$$

$$\leq \sqrt{\text{Tr}(\hat{H}^\dagger H)} \quad \because (\text{Lemma 1 using } \hat{A} = \hat{H}) \tag{S10}$$

Now since the \hat{H} operator is assumed to have elements which are all finite (see definitions in 1.1) (1), and since $\sqrt{\text{Tr}(\hat{H}^\dagger H)}$ is a polynomial on the matrix elements of \hat{H} , one can say $F(\lambda_k, \hat{H}, \hat{O}, |\psi'\rangle)$ in Eq.S9 is always upper-bounded by a finite number (see Eq.S9 and Eq.S10). One should note that $\sqrt{\text{Tr}(\hat{H}^\dagger H)}$ being a trace property is invariant to the choice of basis for expressing the matrix elements of \hat{H} and also independent of any state $|\psi'\rangle$ used for computing $\langle \psi' | \hat{H} | \psi' \rangle$. Also $F(\lambda_k, \hat{H}, \hat{O}, |\psi'\rangle) \geq F(\lambda_k, \hat{H}, \hat{O}, |\psi_k\rangle)$ as $|\psi_k\rangle = \arg \min_{\psi} F(\lambda_k, \hat{H}, \hat{O}, |\psi\rangle)$. This is true for any λ_k as $|\psi_k\rangle$ is the specific minimizer of the cost function in Eq.S1 for that

λ_k and hence will produce a cost-function in Eq.S1 lower in value than with any state $|\psi'\rangle$.

With this information we see

$$\lim_{k \rightarrow \infty} F(\lambda_k, \hat{H}, \hat{O}, |\psi_k\rangle) \leq \sqrt{\text{Tr}(\hat{H}^\dagger H)}$$

$$\lim_{k \rightarrow \infty} \langle \psi_k | \hat{H} | \psi_k \rangle + \lim_{k \rightarrow \infty} \lambda_k \langle \psi_k | (\hat{O} - \omega)^2 | \psi_k \rangle \leq \sqrt{\text{Tr}(\hat{H}^\dagger H)} \quad (\text{S11})$$

$$\lim_{k \rightarrow \infty} \lambda_k \langle \psi_k | (\hat{O} - \omega)^2 | \psi_k \rangle \leq \sqrt{\text{Tr}(\hat{H}^\dagger H)} - \lim_{k \rightarrow \infty} \langle \psi_k | \hat{H} | \psi_k \rangle \quad (\text{S12})$$

$$\lim_{k \rightarrow \infty} \langle \psi_k | (\hat{O} - \omega)^2 | \psi_k \rangle = \langle \psi^* | (\hat{O} - \omega)^2 | \psi^* \rangle = 0 \quad (\lambda_k \rightarrow \infty) \quad (\text{S13})$$

where in arriving at Eq.S13 from Eq.S12 we have used the fact that $\sqrt{\text{Tr}(\hat{H}^\dagger H)}$ is finite (as per definitions 1.1 (1) and the fact that $\sqrt{\text{Tr}(\hat{H}^\dagger H)}$ is a polynomial on the matrix elements of \hat{H}) and $\langle \psi_k | \hat{H} | \psi_k \rangle$ being a quadratic form is also upper-bounded using same Lemma 1 and hence is finite. Thus the RHS of Eq.S12 is a finite-upper bound on the LHS. Only way then the LHS of Eq.S12 can thus stay finite in the limit $\lambda \rightarrow \infty$ is when $\langle \psi_k | (\hat{O} - \omega)^2 | \psi_k \rangle$ is pinned to zero. Since $|\psi^*\rangle = \lim_{k \rightarrow \infty} |\psi_k\rangle$ is the convergent limit point, the result immediately follows. \square

Lemma 3. $\langle \psi^* | (\hat{O} - \omega)^2 | \psi^* \rangle = 0$ if and only if $|\psi^*\rangle \in \text{Null}(\hat{O} - \omega)^2$

Proof. If-part

If $|\psi^*\rangle \in \text{Null}((\hat{O} - \omega)^2)$

$$(\hat{O} - \omega)^2 |\psi^*\rangle = 0 \quad (|\psi^*\rangle \in \text{Null}(\hat{O} - \omega)^2)$$

$$\langle \psi^* | (\hat{O} - \omega)^2 | \psi^* \rangle = 0$$

Only If-part

Let us define a set of eigenvectors of $(\hat{O} - \omega)^2$ as $\{|\eta_i\rangle\}_i$. Since the set is complete one can

expand

$$\begin{aligned}
|\psi^*\rangle &= \sum_i \langle \eta_i | \psi^* \rangle |\eta_i\rangle \\
&= \sum_{|\eta_i\rangle \in \text{Null}((\hat{O}-\omega)^2)} \langle \eta_i | \psi^* \rangle |\eta_i\rangle + \sum_{|\eta_i\rangle \notin \text{Null}((\hat{O}-\omega)^2)} \langle \eta_i | \psi^* \rangle |\eta_i\rangle
\end{aligned} \tag{S14}$$

One can use Eq.S14 in $\langle \psi^* | (\hat{O} - \omega)^2 | \psi^* \rangle$ to arrive at

$$\begin{aligned}
\langle \psi^* | (\hat{O} - \omega)^2 | \psi^* \rangle &= \sum_{|\eta_i\rangle \in \text{Null}((\hat{O}-\omega)^2)} 0 |\langle \eta_i | \psi^* \rangle|^2 + \sum_{|\eta_i\rangle \notin \text{Null}((\hat{O}-\omega)^2)} \eta_i |\langle \eta_i | \psi^* \rangle|^2 \\
&= 0 \quad (\text{by condition}) \\
&\implies \langle \eta_i | \psi^* \rangle = 0 \quad \forall |\eta_i\rangle \notin \text{Null}((\hat{O} - \omega)^2) \quad (\eta_i \geq 0, \text{ see 1.1(2)}) \\
&\implies |\psi^*\rangle \in \text{Null}((\hat{O} - \omega)^2) \quad \because \text{Using Eq.S14}
\end{aligned} \tag{S15}$$

□

Lemma 4. $\text{Null}(\hat{O} - \omega) = \text{Null}((\hat{O} - \omega)^2)$

Proof. This is actually trivial to show. For proof one can see ^{S1}

□

1.2 Theorem 2.1 in main text

Then using the Lemmas above the following is true.

Theorem 1.1. *Let $\{\lambda_i\}_{i=1}^\infty$ be a sequence in the penalty parameter such that $\lambda_1 \leq \lambda_2 \leq \lambda_3 \dots \infty$. Also let $P = \{|\psi_i\rangle\}_{i=1}^\infty$ such that $\forall |\psi_i\rangle \in P$ the following is true.*

$$|\psi_i\rangle = \arg \min_{\psi} F(\lambda_i, \hat{H}, \hat{O}, |\psi\rangle) \tag{S16}$$

In other words P is the set of minimizers for Eq.S1 for each penalty parameter $\lambda \in \{\lambda_i\}_{i=1}^\infty$. If $|\psi^\rangle \in P$ is a limit-point of the convergent sequence $\{\psi_i\}_{i=1}^\infty$ in P i.e $|\psi^*\rangle = \lim_{i \rightarrow \infty} |\psi_i\rangle$ then $|\psi^*\rangle \in S$ (defined in lemma 2)*

Proof. If $|\psi^*\rangle$ is a limit-point of the convergent sequence $\{\psi_i\}^\infty$ in P then

$$\begin{aligned}
\langle \psi^* | (\hat{O} - \omega)^2 | \psi^* \rangle &= 0 && \because \text{see Lemma 2} \\
\implies |\psi^*\rangle &\in \text{Null}((\hat{O} - \omega)^2) && \because \text{see Lemma 3} \\
\implies |\psi^*\rangle &\in \text{Null}((\hat{O} - \omega)) && \because \text{see Lemma 4} \\
\implies |\psi^*\rangle &\in S && \text{(S17)}
\end{aligned}$$

□

2 Deduction of a generic lower bound for successful sampling and characterization of k-parameter

After all the single qubit R_y rotations (parameterized by the bias vectors of the network (\vec{a}, \vec{b})) and Controlled-Controlled Rotations ($C - C - R_y$) targeting the ancillas (parameterized by the interconnecting weights \vec{W} between visible and hidden neurons), the state-vector $|\psi_{v,h,a}\rangle$ of the full set of $(m + n + m \times n)$ qubits is

$$|\psi_{v,h,a}\rangle = \sum_{(\vec{\sigma}, \vec{h})} \sqrt{O(\vec{\sigma}, \vec{h}, \vec{a}, \vec{b})} |\vec{\sigma}\vec{h}\rangle_{vh} \otimes (\sqrt{(1 - \eta(\vec{W}, \vec{\sigma}, \vec{h}))} |\vec{0}\rangle_a + \sqrt{\eta(\vec{W}, \vec{\sigma}, \vec{h})} |\vec{1}\rangle_a) \quad \text{(S18)}$$

where the following definitions is used.

1. $|\psi_{v,h,a}\rangle$ is the combined state of the visible node qubits (abbreviated by subscript v), hidden node qubits (abbreviated by subscript h) and ancilla register (abbreviated by subscript a)
2. $(\vec{\sigma}, \vec{h})$ denotes a sum over the 2^{m+n} bit strings where each $\{\sigma_i\}$ or $\{h_j\} \in \{1, -1\}$
3. $|\vec{\sigma}\vec{h}\rangle_{vh}$ is the 2^{m+n} dimensional state space of n visible node qubits and m hidden node qubits. Note the state $|0\rangle_v$ corresponds to $\sigma_i = -1$ as mentioned in the main text.

Similar statement holds for $h_j = -1$ and $|0\rangle_h$ too.

4. The distribution $O(\vec{\sigma}, \vec{h}, \vec{a}, \vec{b})$ is

$$O(\vec{\sigma}, \vec{h}, \vec{a}, \vec{b}) = \frac{e^{\frac{1}{k}(\sum_i a_i \sigma_i + \sum_j b_j h_j)}}{\sum_{\vec{\sigma}, \vec{h}} e^{\frac{1}{k}(\sum_i a_i \sigma_i + \sum_j b_j h_j)}} \quad (\text{S19})$$

5. The distribution $\eta(\vec{W}, \vec{\sigma}, \vec{h})$ is

$$\eta(\vec{W}, \vec{\sigma}, \vec{h}) = \frac{e^{\frac{1}{k}(\sum_{i,j} w_{ij} \sigma_i h_j)}}{e^{\frac{1}{k} \sum_{i,j} |w_{ij}|}} \quad (\text{S20})$$

6. $|\vec{0}\rangle_a$ and $|\vec{1}\rangle_a$ are the states of the $m \times n$ ancilla qubits (abbreviated as superscript a)

Thus from Eq.S18 we see that when all the qubits are measured, the probability of selecting a bit string $(\vec{\sigma}, \vec{h})$ **and** collapsing the ancilla qubits in state $|\vec{1}\rangle_a$ (only such states are important to this work as they are post-selected after measurement).

$$\begin{aligned} H((\vec{\sigma}, \vec{h}) \cap \vec{1}) &= O(\vec{\sigma}, \vec{h}, \vec{a}, \vec{b}) \eta(\vec{W}, \vec{\sigma}, \vec{h}) \\ &= \frac{e^{\frac{1}{k}(\sum_i a_i \sigma_i + \sum_j b_j h_j)}}{\sum_{\vec{\sigma}, \vec{h}} e^{\frac{1}{k}(\sum_i a_i \sigma_i + \sum_j b_j h_j)}} \times \frac{e^{\frac{1}{k}(\sum_{i,j} w_{ij} \sigma_i h_j)}}{e^{\frac{1}{k} \sum_{i,j} |w_{ij}|}} \end{aligned} \quad (\text{S21})$$

Now successful sampling would be an event wherein all ancilla would collapse to $|\vec{1}\rangle_a$. The probability of such events (denoted as $P_{success} = P(\vec{1}_a)$) irrespective of $(\vec{\sigma}, \vec{h})$ string selected can be obtained by marginalizing $H((\vec{\sigma}, \vec{h}) \cap \vec{1})$ **over all** bit-strings as follows:

$$\begin{aligned}
P_{success} &= P(\vec{1}_a) = \sum_{\vec{\sigma}, \vec{h}} H((\vec{\sigma}, \vec{h}) \cap \vec{1}) \\
&= \sum_{\vec{\sigma}, \vec{h}} \frac{e^{\frac{1}{k}(\sum_i a_i \sigma_i + \sum_j b_j h_j)}}{\sum_{\sigma, h} e^{\frac{1}{k}(\sum_i a_i \sigma_i + \sum_j b_j h_j)}} \times \frac{e^{\frac{1}{k}(\sum_{i,j} w_{ij} \sigma_i h_j)}}{e^{\frac{1}{k} \sum_{i,j} |w_{ij}|}} \\
&= \frac{\langle e^{\frac{1}{k}(\sum_{i,j} w_{ij} \sigma_i h_j)} \rangle_{O(\vec{\sigma}, \vec{h}, \vec{a}, \vec{b})}}{e^{\frac{1}{k} \sum_{i,j} |w_{ij}|}} \\
&\geq \frac{e^{\frac{1}{k}(\sum_{i,j} w_{ij} \langle \sigma_i h_j \rangle_{O(\vec{\sigma}, \vec{h}, \vec{a}, \vec{b})})}}{e^{\frac{1}{k} \sum_{i,j} |w_{ij}|}} \quad \because (\text{Jensen's inequality}) \tag{S22}
\end{aligned}$$

$$\begin{aligned}
\langle \sigma_i h_j \rangle_{O(\vec{\sigma}, \vec{h}, \vec{a}, \vec{b})} &= \sum_{\vec{\sigma}, \vec{h}} O(\vec{\sigma}, \vec{h}, \vec{a}, \vec{b}) \sigma_i h_j \\
&= \sum_{\vec{\sigma}} O_1(\vec{\sigma}, \vec{a}) \sigma_i \sum_{\vec{h}} h_j O_2(\vec{h}, \vec{b}) \quad \because (\text{Eq.S19 } O(\vec{\sigma}, \vec{h}, \vec{a}, \vec{b}) = O_1(\vec{\sigma}, \vec{a}) O_2(\vec{h}, \vec{b})) \\
&= \sum_{\vec{\sigma}} \prod_m O_1(\sigma_m, a_m) \sigma_i \sum_{\vec{h}} h_j \prod_p O_2(h_p, b_p) \quad (\because \text{no intralayer connections as RBM}) \\
&= \sum_{\sigma_i \in \{1, -1\}} O_1(\sigma_i, a_i) \sigma_i \sum_{h_j \in \{1, -1\}} h_j O_2(h_j, b_j) \\
&= \left(\frac{e^{a_i/k} - e^{-a_i/k}}{e^{a_i/k} + e^{-a_i/k}} \right) \left(\frac{e^{b_j/k} - e^{-b_j/k}}{e^{b_j/k} + e^{-b_j/k}} \right) \\
&= \tanh(a_i/k) \tanh(b_j/k) \tag{S23}
\end{aligned}$$

where we have used $\langle \dots \rangle_{O(\vec{\sigma}, \vec{h}, \vec{a}, \vec{b})}$ to denote an average over the distribution $O(\vec{\sigma}, \vec{h}, \vec{a}, \vec{b})$ defined in Eq.S19. Using Eq.S23 in Eq.S22 we thus get

$$\begin{aligned}
P_{success} &= P(\vec{1}_a) \\
&\geq \frac{e^{\frac{1}{k}(\sum_{i,j} w_{ij} \langle \sigma_i h_j \rangle_{O(\vec{\sigma}, \vec{h}, \vec{a}, \vec{b})})}}{e^{\frac{1}{k} \sum_{i,j} |w_{ij}|}} \\
\boxed{P_{success} &\geq \frac{e^{\frac{1}{k}(\sum_{i,j} w_{ij} \tanh(a_i/k) \tanh(b_j/k))}}{e^{\frac{1}{k} \sum_{i,j} |w_{ij}|}} \quad \because \text{Eq.S23}} \tag{S24}
\end{aligned}$$

The above lower bound in Eq.S24 is a generic lower bound independent of any occurrence of random variables $(\vec{\sigma}, \vec{h})$ and only dependant on the parameters of the network $(\vec{a}, \vec{b}, \vec{W})$. From this lower bound all pre-existing known bounds can be recovered as we shall see below

Limiting cases

- $\tanh(a_i/k) \rightarrow \pm 1, \tanh(b_j/k) \rightarrow \pm 1$

In this case we get from Eq.S24

$$\begin{aligned}
P_{success} &= P(\vec{1}_a) \\
&\geq \frac{e^{\frac{1}{k}(\sum_{i,j} w_{ij} \tanh(a_i/k) \tanh(b_j/k))}}{e^{\frac{1}{k} \sum_{i,j} |w_{ij}|}} \\
&\geq \frac{e^{-\frac{1}{k} |(\sum_{i,j} w_{ij} \tanh(a_i/k) \tanh(b_j/k))|}}{e^{\frac{1}{k} \sum_{i,j} |w_{ij}|}} && \because e^{\alpha x} \geq e^{-\alpha|x|} \quad \forall x \in \mathbb{R}, \alpha \geq 0) \\
&\geq \frac{e^{-\frac{1}{k} (\sum_{i,j} |w_{ij}| \tanh(a_i/k) \tanh(b_j/k))}}{e^{\frac{1}{k} \sum_{i,j} |w_{ij}|}} && \because \text{Triangle Inequality} \\
&\geq \frac{e^{-\frac{1}{k} (\sum_{i,j} |w_{ij}| |\tanh(a_i/k)| |\tanh(b_j/k)|)}}{e^{\frac{1}{k} \sum_{i,j} |w_{ij}|}} \\
&\geq \frac{e^{-\frac{1}{k} (\sum_{i,j} |w_{ij}|)}}{e^{\frac{1}{k} \sum_{i,j} |w_{ij}|}} && \because |\tanh(a_i/k)| = |\tanh(b_j/k)| = 1 \\
&\geq \frac{1}{e^{\frac{2}{k} (\sum_{i,j} |w_{ij}|)}} && \tag{S25}
\end{aligned}$$

Thus choosing $k = \max(\sum_{ij} \frac{|w_{ij}|}{2}, 1)$, the lower bound attained in Eq.S25 for the probability for successful sampling becomes a constant value of e^{-4} . This bound was deduced in S2 in a completely different manner. Here we derived a master bound from which this is recovered.

- $\tanh(a_i/k) \rightarrow (a_i/k), \tanh(b_j/k) \rightarrow (b_j/k)$

Using similar kind of reasoning as in the previous case one can show

$$\begin{aligned}
P_{success} &= P(\vec{\mathbb{1}}_a) \\
&\geq \frac{e^{-\frac{1}{k}(\sum_{i,j} |w_{ij}| |\tanh(a_i/k)| |\tanh(b_j/k)|)}}{e^{\frac{1}{k} \sum_{i,j} |w_{ij}|}} \\
&\geq \frac{e^{-\frac{1}{k}(\sum_{i,j} |w_{ij}| |(a_i/k)| |(b_j/k)|)}}{e^{\frac{1}{k} \sum_{i,j} |w_{ij}|}}
\end{aligned}$$

Here one cannot do much to proceed unless some assumptions are made. We assume that $|a_i| \leq a_0 \forall i$ and $|b_j| \leq b_0 \forall j$. Then we get

$$\begin{aligned}
P_{success} &= P(\vec{\mathbb{1}}_a) \\
&\geq \frac{e^{-\frac{1}{k}(\sum_{i,j} |w_{ij}| |(a_i/k)| |(b_j/k)|)}}{e^{\frac{1}{k} \sum_{i,j} |w_{ij}|}} \\
&\geq \frac{e^{-\frac{a_0 b_0}{k^3} (\sum_{i,j} |w_{ij}|)}}{e^{\frac{1}{k} \sum_{i,j} |w_{ij}|}} \\
&\geq \frac{1}{e^{(\frac{1}{k} + \frac{a_0 b_0}{k^3}) (\sum_{i,j} |w_{ij}|)}} \tag{S26}
\end{aligned}$$

One can then numerically choose k to make the bound in this limit in Eq.S26 a constant value greater than a user-defined real number.

3 Hamiltonian for MoS₂ and WS₂

For the Hamiltonian matrix used in this report for MoS₂ and WS₂, we use the 3-band third-nearest neighbor tight-binding description as adopted in Ref.^{S3} The Hamiltonian matrix elements are provided below for brevity and completeness.

The Hamiltonian matrix (\hat{H}) being a 3×3 description is written as

$$\hat{H} = \begin{bmatrix} H_{11} & H_{12} & H_{13} \\ H_{21} & H_{22} & H_{23} \\ H_{31} & H_{32} & H_{33} \end{bmatrix} \quad (\text{S27})$$

Since the Hamiltonian is hermitian ($\hat{H} = \hat{H}^\dagger$), the only unique elements are the upper triangular block. Each such element is described below. For each of the elements we use the symbol $1.0i = \sqrt{-1}$ to denote the imaginary components. Also a_0 is the lattice constant which is 3.190 Å for MoS₂ and 3.191 Å for WS₂^{S3}

$$\begin{aligned}
H_{11} = & \epsilon_1 + 2t_0(2 \cos(\frac{k_x a_0}{2}) \cos(\frac{\sqrt{3}k_y a_0}{2}) + \cos(k_x a_0)) + 2r_0(2 \cos(\frac{3k_x a_0}{2}) \cos(\frac{\sqrt{3}k_y a_0}{2}) + \cos(\sqrt{3}k_y a_0)) \\
& + 2u_0(2 \cos(k_x a_0) \cos(\sqrt{3}k_y a_0) + \cos(2k_x a_0))
\end{aligned}$$

$$\begin{aligned}
H_{12} = & -2\sqrt{3}t_2 \sin(\frac{k_x a_0}{2}) \sin(\frac{\sqrt{3}k_y a_0}{2}) + 2(r_1 + r_2) \sin(\frac{3k_x a_0}{2}) \sin(\frac{\sqrt{3}k_y a_0}{2}) \\
& - 2\sqrt{3}u_2 \sin(k_x a_0) \sin(\sqrt{3}k_y a_0) + 1.0i * 2t_1 \sin(\frac{k_x a_0}{2})(2 \cos(\frac{k_x a_0}{2}) + \cos(\frac{\sqrt{3}k_y a_0}{2})) \\
& + 2(r_1 - r_2)(\sin(\frac{3k_x a_0}{2}) \cos(\frac{\sqrt{3}k_y a_0}{2})) + 2u_1 \sin(k_x a_0)(2 \cos(k_x a_0) + \cos(\sqrt{3}k_y a_0))
\end{aligned}$$

$$\begin{aligned}
H_{13} = & 2t_2(\cos(k_x a_0) - \cos(\frac{\sqrt{3}k_y a_0}{2}) \cos(\frac{k_x a_0}{2})) - \frac{2}{\sqrt{3}}(r_1 + r_2)(\cos(\frac{3k_x a_0}{2}) \cos(\frac{\sqrt{3}k_y a_0}{2}) - \cos(\sqrt{3}k_y a_0)) \\
& + 2u_2(\cos(2k_x a_0) - \cos(k_x a_0) \cos(\sqrt{3}k_y a_0)) + 1.0i * 2\sqrt{3}t_1 \cos(\frac{k_x a_0}{2}) \sin(\frac{\sqrt{3}k_y a_0}{2}) \\
& + \frac{2}{\sqrt{3}}(r_1 - r_2) \sin(\frac{\sqrt{3}k_y a_0}{2})(\cos(\frac{3k_x a_0}{2}) + 2 \cos(\frac{\sqrt{3}k_y a_0}{2})) + 2\sqrt{3}u_1 \cos(k_x a_0) \sin(\sqrt{3}k_y a_0)
\end{aligned}$$

$$\begin{aligned}
H_{22} = & \epsilon_2 + (t_{11} + 3t_{22}) \cos(\frac{k_x a_0}{2}) \cos(\frac{\sqrt{3}k_y a_0}{2}) + 2t_{11} \cos(k_x a_0) + 4r_{11} \cos(\frac{3k_x a_0}{2}) \cos(\frac{\sqrt{3}k_y a_0}{2}) \\
& + 2(r_{11} + \sqrt{3}r_{12}) \cos(\sqrt{3}k_y a_0) + (u_{11} + 3u_{22}) \cos(k_x a_0) \cos(\sqrt{3}k_y a_0) + 2u_{11} \cos(2k_x a_0)
\end{aligned}$$

$$\begin{aligned}
H_{23} = & \sqrt{3}(t_{22} - t_{11}) \sin(k_x a_0) \sin(\sqrt{3}k_y a_0) + 4r_{12} \sin(\frac{3k_x a_0}{2}) \sin(\frac{\sqrt{3}k_y a_0}{2}) \\
& + \sqrt{3}(u_{22} - u_{11}) \sin(k_x a_0) \sin(\sqrt{3}k_y a_0) + 1.0i * 4t_{12} \sin(\frac{k_x a_0}{2})(\cos(\frac{k_x a_0}{2}) - \cos(\frac{\sqrt{3}k_y a_0}{2})) \\
& + 4u_{12} \sin(k_x a_0)(\cos(k_x a_0) - \cos(\sqrt{3}k_y a_0))
\end{aligned}$$

$$\begin{aligned}
H_{33} = & \epsilon_2 + (3t_{11} + t_{22}) \cos(\frac{k_x a_0}{2}) \cos(\frac{\sqrt{3}k_y a_0}{2}) + 2t_{22} \cos(k_x a_0) + 2r_{11}(2 \cos(\frac{3k_x a_0}{2}) \cos(\frac{\sqrt{3}k_y a_0}{2}) \\
& + \cos(\sqrt{3}k_y a_0)) + \frac{2}{\sqrt{3}}r_{12}(4 \cos(\frac{3k_x a_0}{2}) \cos(\frac{\sqrt{3}k_y a_0}{2}) - \cos(\sqrt{3}k_y a_0)) \\
& + (3u_{11} + u_{22}) \cos(k_x a_0) \cos(\sqrt{3}k_y a_0) + 2u_{22} \cos(2k_x a_0) \tag{S28}
\end{aligned}$$

The energy parameter set^{S3} for both the systems MoS₂ and WS₂ is tabulated below

| Parameter List for three-band model from GGA calculations | | |
|---|------------------|-----------------|
| Parameter(eV) | MoS ₂ | WS ₂ |
| ϵ_1 | 0.683 | 0.717 |
| ϵ_2 | 1.707 | 1.916 |
| t_0 | -0.146 | -0.152 |
| t_1 | -0.114 | -0.097 |
| t_2 | 0.506 | 0.590 |
| t_{11} | 0.085 | 0.047 |
| t_{12} | 0.162 | 0.178 |
| t_{22} | 0.073 | 0.016 |
| r_0 | 0.060 | 0.069 |
| r_1 | -0.236 | -0.261 |
| r_2 | 0.067 | 0.107 |
| r_{11} | 0.016 | -0.003 |
| r_{12} | 0.087 | 0.109 |
| u_0 | -0.038 | -0.054 |
| u_1 | 0.046 | 0.045 |
| u_2 | 0.001 | 0.002 |
| u_{11} | 0.266 | 0.325 |
| u_{12} | -0.176 | -0.206 |
| u_{22} | -0.150 | -0.163 |

4 Eigenvectors of L_z and L^2 operator for MoS₂ and WS₂

The L_z operator at K - point in the three-band basis of $(d_{z^2}, d_{xy}, d_{x^2-y^2})$ orbitals of the metal centre is given as^{S3}

$$\hat{L}_z = \begin{bmatrix} 0 & 0 & 0 \\ 0 & 0 & 2i \\ 0 & -2i & 0 \end{bmatrix} \quad (\text{S29})$$

where $i = \sqrt{-1}$. The eigenvectors and eigenvalues of the above matrix is given as

| Eigenvectors and Eigenvalues of L_z operator | | |
|--|-----------------------------------|------------|
| Eigenvalue (ω) | Eigenvector | Band Index |
| -2 | $\frac{1}{\sqrt{2}}[0, -1, -i]^T$ | CB+1 |
| 0 | $[1, 0, 0]^T$ | CB |
| 2 | $\frac{1}{\sqrt{2}}[0, 1, -i]^T$ | VB |

Note that the basis is $d_{z^2} = [1, 0, 0]^T$, $d_{xy} = [0, 1, 0]^T$, $d_{x^2-y^2} = [0, 0, 1]^T$ and the notation VB= valence band (ground state), CB = conduction band (1st excited state) and CB + 1 = Higher energy band (2nd excited state above conduction band). As mentioned in,^{S3} in the chosen basis, the matrix elements of L_x operator and L_y operator are all zeros and hence L^2 operator enjoys exclusive contribution from L_z operator given above. As a result, the eigenvectors of L^2 operator are the same as given in the table above but the eigenvalue pair (-2, 2) of L_z maps to the same eigenspace of L^2 with eigenvalue (ω) =4. In other words L^2 has a doubly-degenerate eigenspace of eigenvalue (ω) =4 made from eigenvectors VB and CB+1 (see Table above) whereas a non-degenerate eigenspace of eigenvalue (ω) =0 with the eigenvector CB (see Table above)

References

- [S1] Axler S. Linear Algebra Done Right, Springer, Cham, 3rd ed., 2015.
- [S2] Xia, Rongxin and Kais, Sabre, Quantum machine learning for electronic structure calculations Nature Communications, 1,4195, 9, **2008**
- [S3] Liu, Gui Bin and Shan, Wen Yu and Yao, Yugui and Yao, Wang and Xiao, Di. Three-band tight-binding model for monolayers of group-VIB transition metal dichalcogenides Physical Review B - Condensed Matter and Materials Physics, 8, 1-11, 88, **2013**